Evaporation from Nanoporous Membranes

by

Kyle Wilke

B.S., Mechanical Engineering (2013)
University of Wisconsin – Madison

MASSACHUSETTS INSTITUTE OF TECHNOLOGY
JUN 14 2016
LIBRARIES
ARCHIVES

Submitted to the Department of Mechanical Engineering in
partial fulfillment of the requirements for the degree of

Master of Science in Mechanical Engineering

at the

MASSACHUSETTS INSTITUTE OF TECHNOLOGY

June 2016

© Massachusetts Institute of Technology 2016
All rights reserved

Author .... Signature redacted ....
Department of Mechanical Engineering
May 20, 2016

Certified by .... Signature redacted ....
Evelyn Wang
Associate Professor of Mechanical Engineering
Thesis Supervisor

Accepted by .... Signature redacted ....
Rohan Abeyaratne
Chairman, Committee on Graduate Students

Evaporation from Nanoporous Membranes

by

Kyle Wilke

Submitted to the Department of Mechanical Engineering on May 20, 2016, in partial fulfillment of the requirements for the degree of Master of Science in Mechanical Engineering.

Abstract

Cooling demands of advanced electronics are increasing rapidly, often exceeding capabilities of conventional thermal management techniques. Thin film evaporation has emerged as one of the most promising thermal management solutions. High heat transfer rates can be achieved in thin films of liquids due to a small conduction resistance through the film to the evaporating interface.

In this thesis, we investigated evaporation from nanoporous membranes. The capillary wicking of the nanopores supplies liquid to the evaporating interface, passively maintaining the thin film. Different evaporation regimes were predicted through modeling and were demonstrated experimentally. Good agreement was shown between the predicted and observed transitions between regimes. Improved heat transfer performance was demonstrated in the pore level evaporation regime over other regimes, with heat transfer rates up to one order of magnitude larger for a given superheat in comparison to the flooding regime.

An improved experimental setup for investigating thin film evaporation from nanopores was developed, where a biphilic membrane, i.e., a membrane with two wetting behaviors, was used for enhanced experimental control to allow characterization of the importance of different design parameters. This improved setup was then used to demonstrate the dependence of thin film evaporation on the location of the meniscus within the nanopores. This dependence on meniscus location within the pore was also shown to increase with increasing superheat. We observed a 46% reduction in heat transfer rates at a superheat of 15 °C for an L^* of 14.67 compared to an L^* of 2, where L^* is the ratio of the depth of the meniscus within the pore to the pore radius.

This work provides practical insights for the design of devices based on nanoporous evaporation. Heat transfer regimes can be predicted based on fluid supply conditions, evaporative heat flux, and membrane geometry. Furthermore, the biphilic membrane serves as a valuable experimental platform for testing the role of membrane geometry on heat transfer performance in the pore level evaporation regime. Future work will focus on demonstrating the importance of different parameters and using experimental results to either validate existing models for evaporation from nanopores or develop more suitable ones.

Thesis Supervisor: Evelyn Wang

Title: Associate Professor of Mechanical Engineering

Acknowledgments

To those that have supported me along the way, it is clear that my experiences up until this point in life would have been very different without you. Though there have been challenges, the unconditional support of loved ones and the guidance and advice of mentors and coworkers has made my time here at MIT so far a truly positive experience. Furthermore, I could not have dreamed of being where I am today without the help/support of everyone. Your presence has not only shaped who I am, but more importantly helped me to pursue my dreams. Regardless of whether or not I know what is beyond the next door in life, knowing who will be there by my side makes it easy to take steps forward and continue to grow as a person. Of that I am forever grateful.

I would like to thank a few members of the Device Research Laboratory specifically (though all have positively impacted my time here so far). First and foremost, my adviser Evelyn Wang, for her guidance, patience, and skills as a mentor. Each meeting ended with me feeling more motivated and in a better mood. I look forward to continuing to work together as I continue my studies. Banafsheh Barabadi for her help and guidance. Zhengmao Lu for advice and discussion on thin film evaporation, and Sungwoo Yang for his expertise with materials. I would also like to thank Kurt Broderick from the Microsystems Technology Laboratories for his willingness to discuss any idea and help in fabrication.

Thank you to the new friends here at MIT that get me out of the office and keep me sane.

Finally, to my family and Alexandra, the love I feel for you only grows. Words cannot describe how privileged I feel to have you all in my life.

Table of Contents

1 INTRODUCTION 16
1.1 MOTIVATION 16
1.2 BACKGROUND 16
1.3 THESIS OBJECTIVES AND OUTLINE 19
2 MEMBRANE DESIGN, FABRICATION, AND CHARACTERIZATION 21
2.1 MEMBRANE DESIGN CONSIDERATIONS 21
2.2 FABRICATION PROCESS 22
2.3 ANODIZED ALUMINUM OXIDE MEMBRANES 22
2.4 RESISTANCE THERMOMETER/HEATER AND CONTACT PAD DEPOSITION AND DESIGN 24
2.4.1 RESISTANCE THERMOMETER/HEATER DEPOSITION 24
2.4.2 MEMBRANE ANNEALING 26
2.4.3 RTD AND HEATER CALIBRATION 26
2.5 BIPHILIC MEMBRANES FOR THIN FILM EVAPORATION 27
2.5.1 PHOTORESIST SOLVENT REDUCTION AND MEMBRANE INFILTRATION 28
2.5.2 PHOTORESIST ETCHING AND SILANE DEPOSITION 29
2.5.3 PHOTORESIST REMOVAL AND MEMBRANE BAKE 30
2.5.4 BIPHILIC MEMBRANE CHARACTERIZATION 30
2.6 SUMMARY 31
3 EXPERIMENTAL SETUP AND PROCEDURE 32
3.1 GOALS FOR THE EXPERIMENTAL SETUP 32
3.2 TEST FIXTURE 33
3.3 EXPERIMENTAL SETUP 35
3.4 MEMBRANE VISUALIZATION 36
3.5 EXPERIMENTAL PROCEDURE 37

3.6 SUMMARY....37

4 MODELING OF DEVICE PERFORMANCE....38

4.1 ENERGY BALANCE ON TEST FIXTURE....38

4.2 FLUID TRANSPORT....39

4.3 MODEL RESULTS....41

4.4 SUMMARY....43

5 EXPERIMENTAL RESULTS....44

5.1 NON-BIPHILIC MEMBRANE EVAPORATION EXPERIMENTS....45

5.1.1 FLOODING REGIME....45

5.1.2 TRANSITION REGIME....45

5.1.3 PORE LEVEL EVAPORATION REGIME....46

5.1.4 LIMITED FLUID SUPPLY REGIME....48

5.2 BIPHILIC MEMBRANE EVAPORATION EXPERIMENTS....50

5.2.1 EFFECT OF MENISCUS LOCATION WITHIN PORE....50

5.3 SUMMARY....53

6 CONCLUSIONS....54

6.1 CONTRIBUTIONS....54

6.2 RECOMMENDATIONS FOR FUTURE WORK....55

7 REFERENCES....56

8 APPENDIX....59

ELECTROLYSIS....59

PORE DISTRIBUTION CORRECTION....59

NON-CIRCULAR CROSS SECTION....60

BOILING SUPRESSION WITHIN PORE....61

VAPOR FLOW REGIME....62

MEMBRANE PARAMETERS....63

CALCULATION OF ERROR..64

List of Figures

Figure 1: a) CPU power density over time highlighting rapid increases. [1] b) Infrared temperature map of a GaN HEMT depicting highly localized heat generation during operation. [2] 16

Figure 2: Schematic of a thin film region of an evaporating meniscus in a microchannel. The meniscus is typically split into three regions: a non-evaporating adsorbed film region, an evaporating thin film region, and the intrinsic meniscus region where the film is considerably thicker. [13] 18

Figure 3: Schematic of evaporation from a nanoporous membrane. Liquid is wicked from the bottom to the evaporating interface via capillarity. Heat conduction through the liquid is small due to the small pore diameter. 18

Figure 4: Schematic of a nanoporous membrane with thickness t and pore diameter D. 21

Figure 5: SEM images top view of typical AAO membrane with a pore diameter of 150 nm. (scale bars: 200 nm) a) top view. b) cross sectional view of AAO membrane. 23

Figure 6: Top view SEM image of an AAO membrane after exposure to water at 100° C. (scale bar: 1 µm) Reactions with water altered membrane structure significantly. 24

Figure 7: SEM images of different thicknesses of platinum RTDs and heaters deposited on the surface of AAO membranes via electron beam deposition. (scale bars: 100 nm) A continuous network was formed in both but when the layer becomes more than a few tens of nanometers pores begin to be closed off by the platinum. a) 25 nm thick. b) 125 nm thick. 25

Figure 8: Cross section SEM images of 25 nm of platinum deposited on the membrane surface for different deposition angles. An increased deposition angle decreases the distance platinum is deposited within the pores. (scale bars: 200 nm) a) deposition angle 0°. b) deposition angle 30°. 25

Figure 9: Top view SEM images of membranes before and after annealing at 350° C highlighting the morphology change. (scale bars: 100 nm) a) RTD before. b) RTD after. c) contact pad before. d) contact pad after. 26

Figure 10: Typical calibration for the platinum RTD. Resistance increases linearly with increasing temperature. 27

Figure 11: Optical image of nanoporous membrane after RTD and contact pad deposition. (scale bar: 5 mm) 27

Figure 12: a) Cross section view of membrane at surface. The pores widen at the top surface. (scale bar: 200 nm) b) schematic of desired wetting properties. The hydrophobic layer prevents liquid from flooding the membrane surface. It also prevents the liquid vapor interface from forming at the location where the pores widen. 28

Figure 13: Cross section SEM image of a membrane filled with photoresist, showing pores completely filled up to the membrane surface. (scale bar: 1 µm) 29

Figure 14: a) 100 nm pore diameter AAO membrane infiltrated with photoresist after being etched in an air plasma for 30 min. b) Etch depth plotted against etch time for different pore diameter membranes. Error bars represent the standard deviation of etch depth across samples at a given time point 29

Figure 15: Optical images of a drop of water on the top and bottom surfaces of the biphilic membrane. The bottom is hydrophilic while the top is hydrophobic. (scale bar: 5 mm) 30

Figure 16: Cross section SEM images of membranes filled with 5 nm gold nanoparticles after biphilic treatment for different photoresist etch times. The onset of the hydrophobic section is shown as an orange line. Gold nanoparticles (appear as bright spots within the pores) are not found within this section but are found below it. a) shorter etch time. b) longer etch time. (scale bars: 100 nm) 31

Figure 17: a) Exploded view of test fixture, depicting fluid inlets and outlets, measurement ports, and membrane location. b) Optical image of test fixture looking down from topside. In the middle the membrane is sealed between two O-rings. (scale bar: 1 cm) 34

Figure 18: Schematic of cross section of test fixture and membrane. 35

Figure 19: a) Schematic of experimental setup. b) Optical image of test setup inside vacuum chamber through camera viewport. (scale bar: 1 cm) 35

Figure 20: a) Test fixture as seen through camera viewport. b) Membrane flooded with liquid. The dark region at the bottom is a thick layer of liquid building up. c) Membrane where heating of the surface has caused flooding to stop for a portion of the surface but flooding still remains along the bottom and sides of the membrane. d) Heating power is great enough that no flooding remains. (scale bars: 5 mm) 36

Figure 21: Control volume around test fixture with inlet, outlet, and generation terms. 38

Figure 22: Characterization of losses from test fixture. Loss mechanisms included radiation and convection on the vapor side of the membrane, conduction through the test fixture, as well as sensible heating of the fluid below the membrane 39

Figure 23: Schematic of different pressures and pressure drops relevant to liquid supply to the evaporating interface..40

Figure 24: Membrane flood rate compared to pore radius. Experimental data points are plotted along with the model prediction. Error bars represent the root mean squared error, with the dominant error stemming from uncertainty in the membrane porosity. (*normalized by pore area).........41

Figure 25: Possible wetting and heat transfer regimes. a) Flooding regime where fluid accumulates on the membrane surface. b) Pore level evaporation regime where fluid supply and evaporation rate balance. c) Limited fluid supply regime where fluid supply is inadequate to supply liquid to the membrane surface..42

Figure 26: Different heat transfer regimes for evaporation from a nanoporous membrane as a function of the evaporative heat flux and pore radius. (Fluid – Water, T = 22° C, P_{supply} = 1 atm, normalized by pore area)..43

Figure 27: Evaporative heat flux compared to surface superheat for different pore diameter samples and water as the working fluid. (*normalized by total area) 44

Figure 28: a) Optical image of membrane in flooding regime. (scale bar: 5 mm) b) Evaporative heat flux compared to membrane surface superheat in flooding regime for 75 nm pore radius sample and water as working fluid. (*normalized by total area)...45

Figure 29: a) Optical image of membrane in transition regime. (scale bar: 5 mm) b) Surface temperature RTD measurements over time for a set heat flux in the transition regime. The surface fluctuates between a high temperature and low temperature as the amount of fluid flooding the surface increases and decreases. 46

Figure 30: a) Optical image of membrane surface during pore level evaporation regime. (scale bar: 5 mm) b) Evaporative heat flux determined via an energy balance on the test fixture compared to the heat flux input by the platinum heater. When these data points fall on a 45 degree line thin film evaporation has been reached. (*normalized by total area) 47

Figure 31: Evaporative heat flux compared to surface superheat for water evaporated into saturated vapor at 22° C and a supply pressure of 1 atm. a) (*normalized by total area) b) (*normalized by pore area)..48

Figure 32: a) Different heat transfer regimes for evaporation from a nanoporous membrane as a function of the evaporative heat flux and pore radius. (Fluid – Water, Isopropanol, T = 22° C, P_{supply} = 1 atm, normalized by pore area) b) Evaporative heat flux for isopropanol determined via an energy balance on the test fixture plotted against the heat flux input by the platinum heater.

When these data points fall on a 45 degree line thin film evaporation has been reached. (*normalized by total area) 49

Figure 33: Evaporative heat flux compared to surface superheat (*normalized by total area) for evaporation of isopropanol into saturated vapor at 22° C with a supply pressure of 1 atm. 50

Figure 34: Evaporative heat flux compared to surface superheat (*normalized by pore area) for evaporation of water into saturated vapor at 22° C with a supply pressure of 1 atm with a biphilic membrane. Tests are run with membranes with three different L*. Dashed lines are from the model framework presented in [36]. 51

Figure 35: Evaporative heat flux plotted against L* for different superheats (*normalized by pore area). Tests are conducted evaporating into saturated vapor at 22° C with a supply pressure of 1 atm with a biphilic membrane. Tests are run on membranes with three different L*. Dashed lines are from the model framework presented in [36] 52

Figure 36: a) open circuit RTD and heater on membrane for electrolysis tests. b) Measured current vs applied voltage during electrolysis tests. 59

Figure 37: Mass flow rate corrections for a normal pore distribution with a standard deviation of 13% of mean pore radius. Blue is for purely flooding case. Orange is for purely capillary driven flow. Yellow is for a combination of capillary and supply pressure driven flow (Eq. 12). 60

Figure 38: The ratio of the capillary pressure, viscous pressure drop, and fluid flow rate in an elliptical pore to that of a circular pore of the same cross section as a function of the ratio of one axis of the ellipse to the radius of the circle. 61

Figure 39: Knudsen number for 150nm, 100nm, and 80 nm pore diameter samples for different temperatures. The Knudsen number was 10 or higher for most tests, ensuring the accuracy of the ballistic transport assumption. 62

1 INTRODUCTION

1.1 MOTIVATION

The continued push for higher performance electronics, as well as the development of new technologies, is creating devices with significant thermal management needs. Figure 1a shows the rapid increase in CPU power densities over time. [1] Increases in device power density often go hand in hand with the amount of heat that needs to be dissipated from a given area of the device. Figure 1b shows an infrared temperature map of a gallium nitride (GaN) HEMT. [2] The image highlights how heat generation is often highly localized, creating regions where extremely high heat fluxes must be dissipated. The need for improved thermal management systems is not limited to CPUs and GaN HEMTS, but is also important in other areas such as power amplifiers, concentrated solar photovoltaics, and laser diodes. Some emerging electronics are even reported to produce heat fluxes greater than 1000 W/cm^2. [3, 4] Conventional cooling methods, however, have critical heat fluxes (the maximum heat flux that can be dissipated by a given technology) of around 100 W/cm^2 or less and are quickly becoming inadequate. [5] Therefore, the improvements in current device performance and the creation of new electronics requires the simultaneous development of alternative thermal management solutions capable of dissipating large heat fluxes.

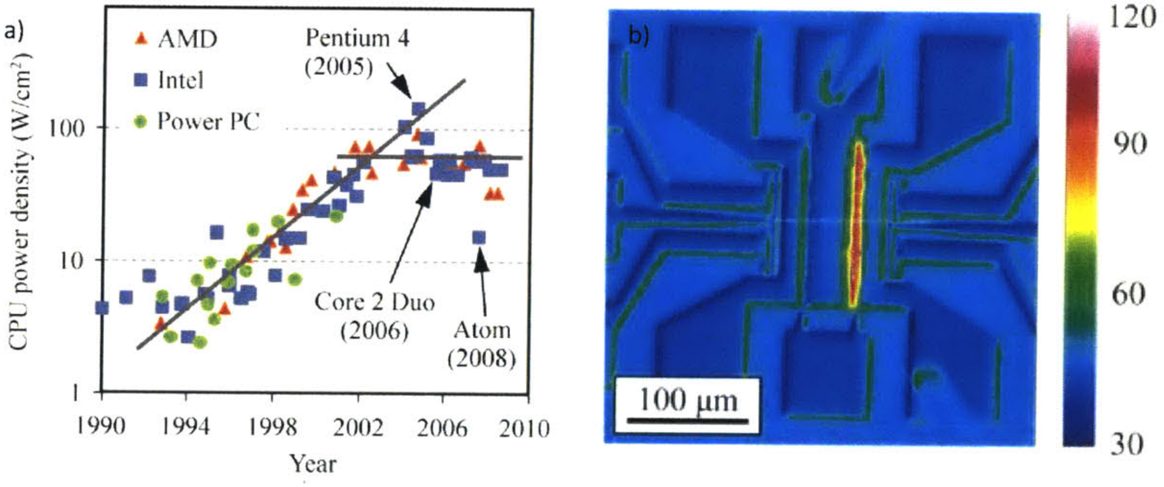

Figure 1: a) CPU power density over time highlighting rapid increases. [1] b) Infrared temperature map of a GaN HEMT depicting highly localized heat generation during operation. [2]

1.2 BACKGROUND

A number of methods to dissipate high heat fluxes are actively being researched. These methods predominately focus on utilizing the large latent heat of vaporization, whereas conventional methods are dominated by single phase technologies. Methods currently being researched include pool boiling, flow boiling, jet impingement, and thin film evaporation. Each of which have different requirements and advantages. Pool boiling does not require any pumping power and can dissipate heat fluxes in excess of 100 W/cm^2. [6] However, at the critical heat flux (CHF) the heat transfer performance is reduced drastically due to the transition to film boiling. Therefore, much work has focused on increasing the CHF. [6-8] In flow boiling, fluid is pumped through channels and heat fluxes up to 300 W/cm^2 have been demonstrated. [9] This technique suffers from instabilities that limit performance, and can have significant pumping requirements. [10, 11] Jet impingement relies on high velocity jets of liquid hitting the hot surface. Heat fluxes up to 500 W/cm^2 have been demonstrated, but significant pumping power is needed. [12]

Thin film evaporation, the focus of this thesis, is a promising method for efficiently dissipating high heat fluxes due to the possibility of having a large CHF, not requiring significant pumping power, and avoiding flow instabilities. As the name implies, thin film evaporation involves transferring heat through a thin film of liquid to an evaporating interface. When the film is thin enough (around 1 µm for most fluids), the conduction resistance across the liquid film becomes approximately the same magnitude as the interfacial resistance to evaporation. This allows the potential of the evaporative interface to be fully utilized in thin films, enabling large heat transfer coefficients. Figure 2 depicts the thin film region of a meniscus within a microchannel, where near the leading edge of the meniscus the film becomes very thin. [13] The potential for an efficient means of heat dissipation has led to significant interest in evaporating thin films. [14-24] Different nano/micro wicks have been investigated to maintain the thin film, and heat fluxes up to 550 W/cm^2 have been demonstrated. [25-27] However, thin films have inherently large viscous losses which can limit the performance of passively driven thin film evaporation. [28]

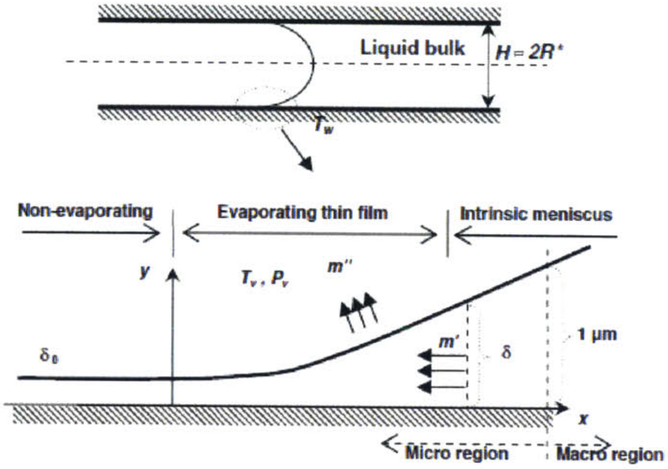
Liquid bulk
H = 2R*
T_w
Non-evaporating
Evaporating thin film
Intrinsic meniscus
y
T_v, P_v
m''
m'
δ
1 μm
δ_0
x
Micro region
Macro region

Figure 2: Schematic of a thin film region of an evaporating meniscus in a microchannel. The meniscus is typically split into three regions: a non-evaporating adsorbed film region, an evaporating thin film region, and the intrinsic meniscus region where the film is considerably thicker. [13]

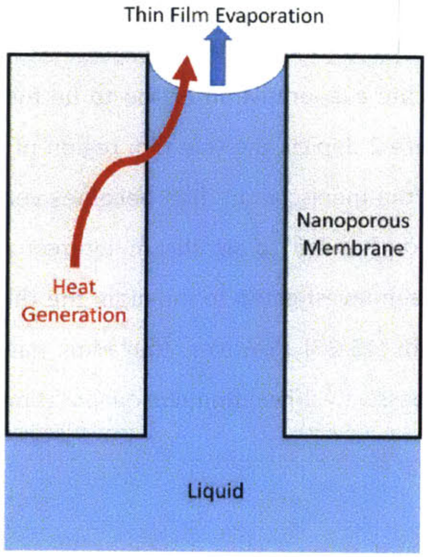
Thin Film Evaporation
Nanoporous Membrane
Heat Generation
Liquid

Figure 3: Schematic of evaporation from a nanoporous membrane. Liquid is wicked from the bottom to the evaporating interface via capillarity. Heat conduction through the liquid is small due to the small pore diameter.

If the microchannel is made small enough, every location on the liquid-vapor interface can be less than 1 μm from the channel wall, allowing the entire interface to act as an evaporating thin film with large heat transfer coefficients. This can be achieved by utilizing a nanoporous membrane, as depicted in Figure 3. In this system the fluid is passively supplied to the evaporating interface via capillary pressure generated by the liquid-vapor interface. The nanoporous membrane can be made out of a high conductivity material and integrated directly with the device requiring heat dissipation. This provides a low resistance conduction path from the heat source to the evaporating interface. Finally, because the liquid is confined within a nanopore, the furthest heat must conduct through the liquid (typically poor thermal conductivity) is small. Subsequently, the conduction resistance to heat transfer is small and does not limit the heat dissipation process, satisfying the thin film evaporation requirement.

A cooling scheme utilizing a nanoporous membrane to constrain a film of liquid between the membrane from which thin film evaporation can occur and a heater below has previously been proposed and promising heat transfer results demonstrated (net heat fluxes exceeding 500 W/cm^2) [29-31] It was also suggested that the large viscous resistance to liquid flow generally coupled with flow through nanopores could be decoupled from the large capillary pressures generated in the nanopores by using a thin membrane, making it possible to achieve extremely high heat flux dissipation, overcoming one practical limitation to thin film evaporation. [32] This concept was used to model and design a practical system for high heat flux dissipation (in excess of 1000 W/cm^2). [33, 34] A number of models have also been developed to investigate evaporation from nanopores. The combined effect of electrostatic and van der Waals forces on evaporation from nanopores was considered, where it was found that these forces enhance the evaporation rate per unit pore area, but it was noted that the capillary force is still the dominant force at pore radii as small as 30 nm. [35] A framework for modeling evaporation from nanopores considering deviations from the classical kinetic theory was also presented, in which the potential for the interface shape and location of the meniscus to regulate the fluid supply was considered, as well as the role of other geometric parameters such as pore diameter and porosity. [36]

1.3 THESIS OBJECTIVES AND OUTLINE

Though there have been experimental works demonstrating the potential of thin film evaporation from nanopores, there has been little experimental work to support the findings of theoretical works to design devices and investigate the significance of different parameters.

The objective of this thesis is to enhance the understanding of how evaporation from nanopores responds to a variety of design conditions set forth in previous modeling works, such as geometric parameters including pore diameter, porosity, and meniscus location within the pore, as well as system properties such as fluid choice, liquid supply pressure, etc. The structure of the thesis is outlined below.

In Chapter 1, background information and motivation for the current research is presented. This information is used to establish the goals of this thesis.

In Chapter 2, the fabrication and characterization of nanoporous membranes used in this work is presented.

In Chapter 3, an experimental setup is developed and described for accurately probing thin film evaporation.

In Chapter 4, a simple model of liquid transport to the evaporating interface and an energy balance on the experimental setup is developed to help understand and analyze experimental results.

In Chapter 5, experimental results are discussed and analyzed using the simple models presented in Chapter 4. In some cases the results are also compared to previous modeling works on thin film evaporation from nanopores.

In Chapter 6, conclusions are drawn and future work is proposed.

2 MEMBRANE DESIGN, FABRICATION, AND CHARACTERIZATION

2.1 MEMBRANE DESIGN CONSIDERATIONS

Before designing a membrane fabrication process, desired geometric parameter ranges for testing were considered. Figure 4 depicts a nanoporous membrane where *t* is the membrane thickness and *D* is the pore diameter.

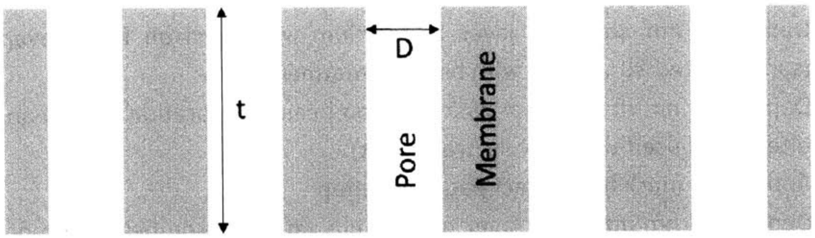

Figure 4: Schematic of a nanoporous membrane with thickness t and pore diameter D.

The capillary pressure and viscous pressure drop are both a function of pore diameter. Furthermore, a small pore diameter is needed to satisfy the thin film evaporation requirement. Previous design studies have suggested using pore diameters on the order of 100 nm or smaller to maximize the capillary pressure, and modeling work has also focused on this length scale. [34] Therefore, this work will examine pore diameters in this range as well.

The viscous pressure drop scales linearly with the membrane thickness. The thicker the membrane is the larger the resistance to fluid transport across the membrane. Therefore, to achieve very high heat fluxes thin membranes must be used. In this study, however, we are interested in the behavior of evaporation from nanopores as opposed to demonstrating extremely high heat flux dissipation. Therefore, an intermediate membrane thickness of 100 µm was chosen to maintain membrane mechanical stability during tests and allow a limited fluid supply regime to be reached. Previous works designing membrane based evaporators suggested using membranes sub-micron in thickness to maximize potential heat flux dissipation. [32, 34]

Finally, membrane porosity is also important. Porosity is defined as the ratio of pore area to the total area of a membrane. Therefore, a larger porosity means more pore area and in turn more evaporative area. As such, recent modeling works have suggested that larger porosities are better for achieving large heat fluxes. [36] However, fabrication of very high porosity nanoporous membranes that are also mechanically stable is challenging. Therefore, this study will use porosities of 0.35 or less.

2.2 FABRICATION PROCESS

The complete fabrication procedure is first listed in its entirety. The steps and characterization are then described in further detail in Chapter 2 subsections to follow.

1. Purchase AAO membranes with desired geometry
2. Fabricate resistance thermometer(RTD)/heater and contact pad
    a. Apply hard mask for RTD deposition
    b. Deposit 5 nm adhesion layer of titanium with electron beam evaporation for RTD (sample tilted 30° if used with biphilic treatment)
    c. Deposit 25 nm of platinum with electron beam evaporation as RTD and heater (sample tilted 30° if used with biphilic treatment)
    d. Apply hard mask for contact pad deposition
    e. Deposit 25 nm adhesion layer of titanium with electron beam evaporation for contact pad
    f. Deposit 400 nm of gold with electron beam evaporation as contact pad
    g. Thermally anneal membranes at 350° C for 3hrs
3. Create biphilic membrane (if used)
    a. Vacuum desiccate AZ5214 for 16 hr to lower solvent content
    b. Place membrane on 18 µL drop of photoresist with side to be made hydrophobic (RTD side) facing up
    c. Wait two hours to allow photoresist to fully infiltrate pores
    d. Bake at 90° C for 50 min
    e. Etch photoresist with air plasma to expose pores desired amount
    f. Wash for ~1 min in 5 weight percent phosphoric acid in water
    g. Place in vacuum desiccator with 200 µL perfluorodecyltrichlorsilane for 3 hr
    h. Rinse with acetone for ~5 min to remove bulk of photoresist
    i. Rinse with microstrip 2001 at 60° C for 30 min to remove any remaining photoresist
    j. Rinse with water
    k. Bake at 90° C for 8 hr
4. Calibrate RTD
    a. Place membrane in test fixture with RTD and heater connections attached
    b. Place in oven, set temperature at increments of 20° C between 20° C and 80° C and record sample resistance

2.3 ANODIZED ALUMINUM OXIDE MEMBRANES

Anodized aluminum oxide (AAO) membranes were chosen due to the flexibility in selecting parameters to vary as well as the well-controlled geometry they provide. AAO membranes were fabricated from high purity aluminum through an anodization process that produces well ordered, high-aspect ratio, cylindrical pores. Membranes were purchased from Synkera Technologies Inc. and were available in pore sizes ranging from 10 nm up to 200 nm. Pore spacing could also be controlled, providing control over the membrane porosity up to approximately 38%. Figure 5a and b are scanning electron microscope (SEM) images of representative nanoporous membranes, showing a top view and cross sectional view, respectively. The images show the well-ordered cylindrical nanopores typical of AAO membranes. Membrane porosity and pore diameter were confirmed via image processing of SEM images.

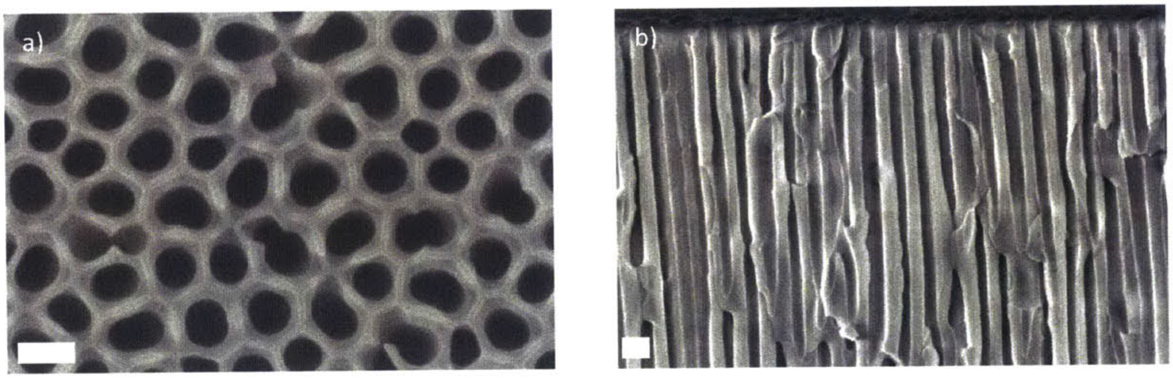

Figure 5: SEM images top view of typical AAO membrane with a pore diameter of 150 nm. (scale bars: 200 nm) a) top view. b) cross sectional view of AAO membrane.

The alumina of the AAO membranes was in the amorphous phase when purchased. The stability of the AAO membranes in the working fluids used in this study was first tested. Figure 6 shows a top view SEM image of a membrane after exposure to boiling water at 100° C. The membrane structure was completely altered. A number of methods of avoiding reactions with water were explored, including high temperature annealing which changes the phase of the alumina, as well as atomic layer deposition (ALD) of a protective layer of hafnia. The high temperature annealing process, however, caused the membranes to become brittle and difficult to work with, and the ALD process was unable to coat the entirety of the high aspect ratio pore due to limitations of the ALD system. Therefore, all experiments with water were kept below a temperature of 65° C, for which no change in membrane structure was observed after a 3 hr exposure to water. No reaction was observed with other working fluids used in this study.

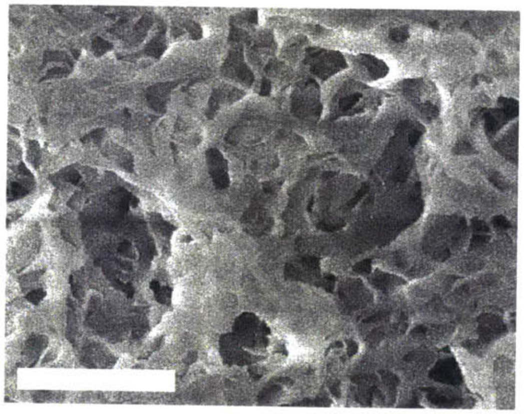

Figure 6: Top view SEM image of an AAO membrane after exposure to water at 100° C. (scale bar: 1 μm) Reactions with water altered membrane structure significantly.

2.4 RESISTANCE THERMOMETER/HEATER AND CONTACT PAD DEPOSITION AND DESIGN

2.4.1 RESISTANCE THERMOMETER/HEATER DEPOSITION

Figure 7a and b show top view SEM images of 25 nm and 125 nm of platinum deposited on the membrane surface to be used as a resistance thermometer (RTD) and heater. Deposition was done using electron beam evaporation (ATC E-Beam Evaporation System, AJA). This deposition technique was chosen due to its high degree of directionality, which helps prevent the pores from clogging or being closed off by the deposited material. The layers were deposited on top of a 5 nm titanium adhesion layer. A continuous network of platinum was formed without significantly altering the pore geometry when thicknesses on the order of 25 nm are deposited. However, when the deposited RTD thickness became too large, the pores started to close off as seen in the SEM image of 125 nm of deposited platinum. This issue of closing off the pores was also more severe when smaller pore diameters were used. Therefore, an RTD thickness of ~25 nm was used in all tests to ensure a continuous network of platinum was deposited while preventing any alteration of pore geometry.

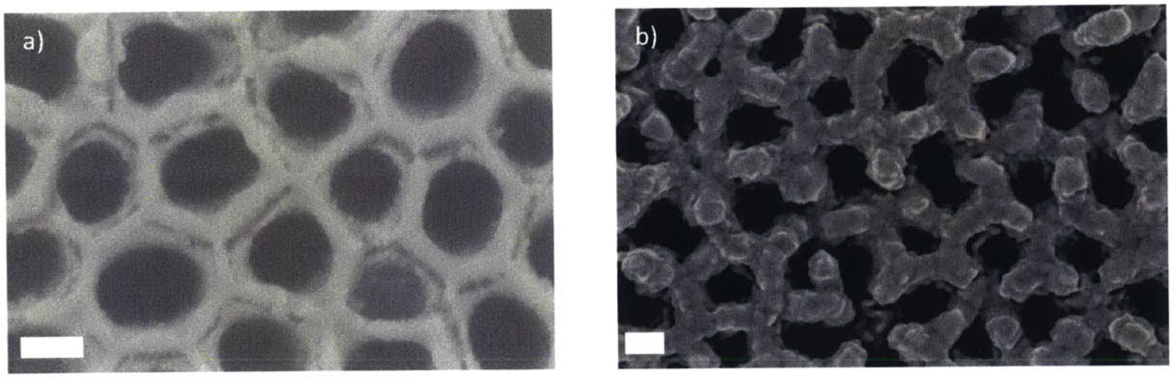

Figure 7: SEM images of different thicknesses of platinum RTDs and heaters deposited on the surface of AAO membranes via electron beam deposition. (scale bars: 100 nm) A continuous network was formed in both but when the layer becomes more than a few tens of nanometers pores begin to be closed off by the platinum. a) 25 nm thick. b) 125 nm thick.

Though pore geometry was preserved, some platinum was able to deposit within the pores. When further processing (biphilic membrane) was necessary, RTD deposition was done with the membrane at an angle 30° from normal. Due to the directionality of electron beam deposition, the angled deposition prevented material from depositing deep within the pore and prevented any unknown complications from occurring during subsequent processing. Figure 8a and b show cross sectional SEM images of membranes after RTD deposition normal to the surface and 30° off normal, respectively. When platinum was deposited at an angle of 30° to normal, material was only deposited a couple hundred of nanometers into the pore. However, when no angle was used during deposition, material could be found up to a couple micrometers into the pore.

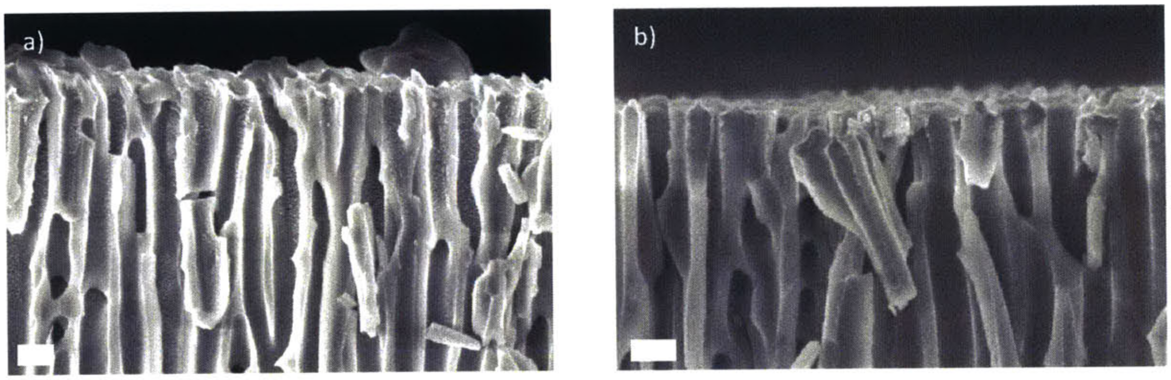

Figure 8: Cross section SEM images of 25 nm of platinum deposited on the membrane surface for different deposition angles. An increased deposition angle decreases the distance platinum is deposited within the pores. (scale bars: 200 nm) a) deposition angle 0°. b) deposition angle 30°.

The RTD and heater shape was defined by a hard mask. After deposition of the RTD and heater, the hard mask was exchanged with a second hard mask to define the contact pad geometry. 25 nm of titanium was first deposited as an adhesion layer and then 400 nm of gold as the contact pad.

2.4.2 MEMBRANE ANNEALING

The membranes with RTDs were then annealed at 350° C for 3 hours. This annealing process was done at temperatures much higher than what the membranes were operated at during experiments, preventing changes in morphology/resistance of the films that could lead to measurement error during tests. Figure 9a-d shows SEM images of the RTD and contact pads before and after the thermal annealing process, highlighting the large changes in structure of the deposited materials and the importance of this fabrication step.

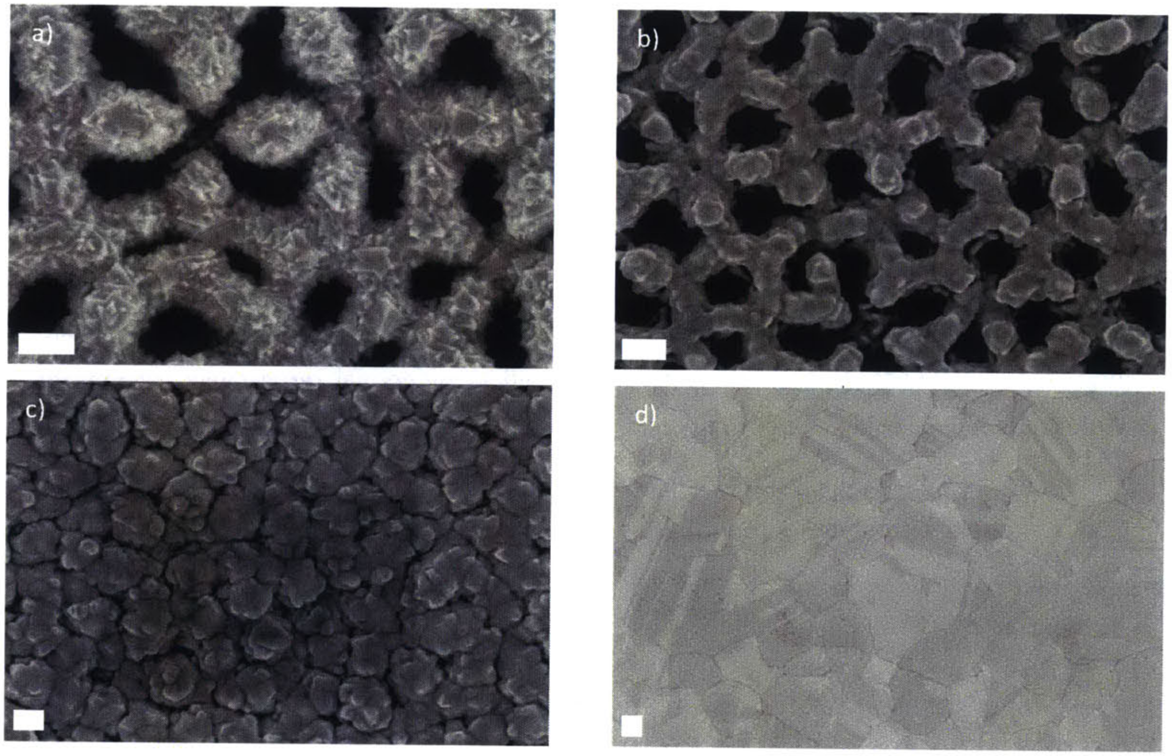

Figure 9: Top view SEM images of membranes before and after annealing at 350° C highlighting the morphology change. (scale bars: 100 nm) a) RTD before. b) RTD after. c) contact pad before. d) contact pad after.

2.4.3 RTD AND HEATER CALIBRATION

During experimental tests, the temperature of the evaporating interface was monitored. The layer of platinum was used as a resistance thermometer (RTD) while simultaneously providing the heating for evaporation. RTD calibrations were performed on all samples before testing to determine the temperature dependent resistance of the platinum layer. Figure 10 shows the calibration for a typical sample. The samples all had positive temperature dependence with typical temperature coefficients between 0.0011° C^{-1} and 0.0017° C^{-1}. This value was considerably less than the bulk value for platinum (0.003927° C^{-1}), however, this was not surprising due to the fact that very thin layers were used. The

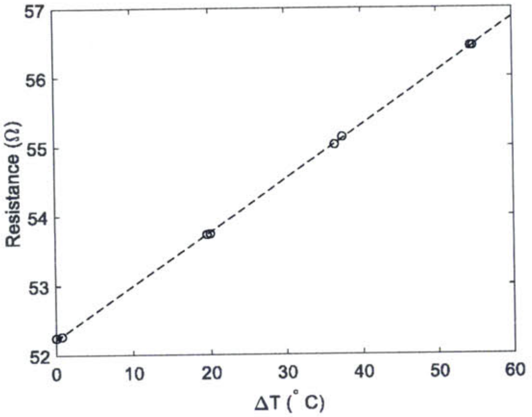

Figure 10: Typical calibration for the platinum RTD. Resistance increases linearly with increasing temperature.

RTDs showed repeatable, linear responses in resistance with changes in temperature, allowing for a reliable measurement of the surface temperature.

Figure 11 shows an optical image of a nanoporous membrane after RTD and contact pad deposition. Numerous RTD designs were tested. It was found that a uniform RTD layer over the entire surface and a wide, thick contact pad produced the most uniform heating, as opposed to, for example, a serpentine RTD design. No RTD and heater material was deposited where the O-rings would be touching the membrane to prevent heating at locations without evaporation, which could lead to measurement error.

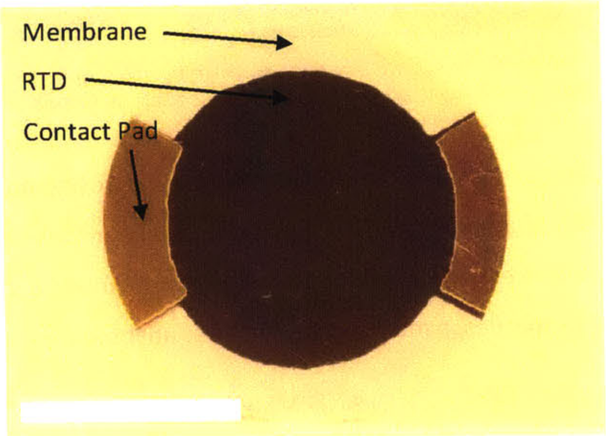

Figure 11: Optical image of nanoporous membrane after RTD and contact pad deposition. (scale bar: 5 mm)

2.5 BIPHILIC MEMBRANES FOR THIN FILM EVAPORATION

For certain tests improved control over the liquid vapor interface was desired. This was due to multiple reasons. The first was that during certain tests, liquid was able to flood the surface completely. In this situation, there was no liquid vapor interface within the pore, and thin film evaporation was not possible. The second reason is shown in Figure 12a and b. In Figure 12a, a cross section image of the membrane at the surface shows that at the very surface of the membrane the pores widen. This creates uncertainty in the pore diameter and membrane porosity for different samples. A couple hundred nanometers within the pore, however, the geometry was found to be much more consistent and could be characterized with better certainty. Figure 12b depicts the desired wetting properties, where a biphilic membrane (membrane with two wetting properties, one philic, and one phobic) allows liquid to wick into the membrane from the bottom. However, when the liquid reaches the phobic section it becomes pinned. This prevented the membrane surface from flooding, as well as maintained the liquid below the section of the pore with uncertain geometry.

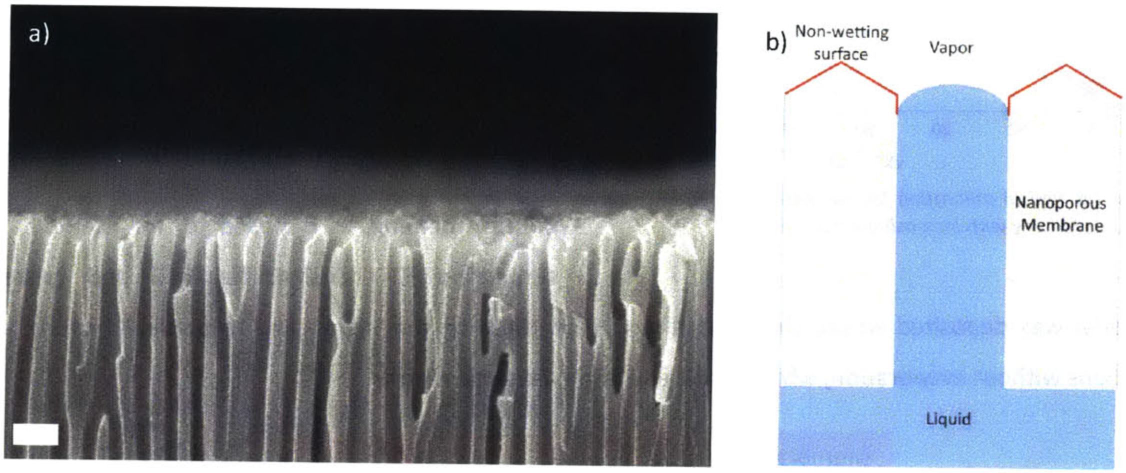

Figure 12: a) Cross section view of membrane at surface. The pores widen at the top surface. (scale bar: 200 nm) b) schematic of desired wetting properties. The hydrophobic layer prevents liquid from flooding the membrane surface. It also prevents the liquid vapor interface from forming at the location where the pores widen.

By creating a biphilic membrane, parameters such as membrane porosity, pore diameter, and wetting location within the pore could be studied. These parameters have been looked at through modeling and could be studied for the first time experimentally with the biphilic membrane described here. In order to achieve the desired wetting properties, a multistep process was adapted from work by Lee *et al.* [37]

2.5.1 PHOTORESIST SOLVENT REDUCTION AND MEMBRANE INFILTRATION

To begin, 3 mL of the photoresist AZ5214 was placed in a vacuum desiccator for 16 hr to reduce the solvent content. This prevented bubbles from forming within the pores when the solvent was evaporated off in later steps.

The membranes were then placed on top of an 18 μL drop of photoresist on a glass slide. The face to be made non-wetting was placed facing up. The photoresist was then given 2 hr to infiltrate the pores completely. After infiltration the membranes were baked at 90° C to remove any remaining solvent. The top surface of the membranes were just covered by the photoresist a few hundred nanometers thick and the pores were completely filled, as seen in the cross section view of an infiltrated membrane in Figure 13.

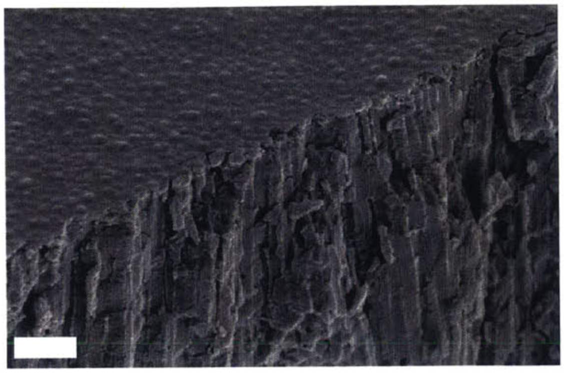

Figure 13: Cross section SEM image of a membrane filled with photoresist, showing pores completely filled up to the membrane surface. (scale bar: 1 μm)

2.5.2 PHOTORESIST ETCHING AND SILANE DEPOSITION

After being filled with photoresist, the top section of the pores was exposed by etching the photoresist with an air plasma at 700 mTorr using a plasma cleaner (Expanded Plasma Cleaner PDC-001, Harrick Plasma) set at low RF power. Figure 14a shows a cross section SEM image of a 100 nm pore diameter AAO membrane filled with photoresist after being etched for 30 min. The top surface and beginning of the pores was exposed down to a depth of a couple hundred nanometers. Figure 14b shows the etch time necessary to achieve a certain etch depth for different pore diameters relevant to this thin film evaporation study.

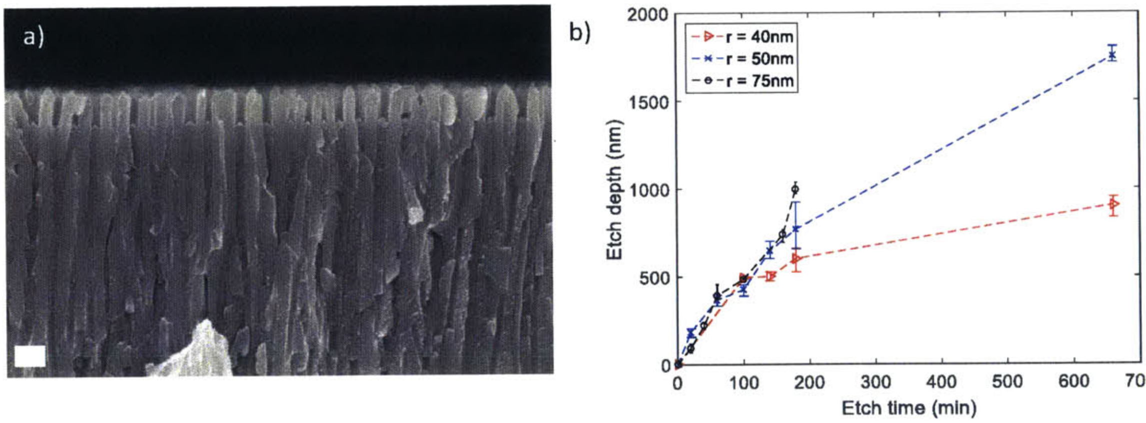

Figure 14: a) 100 nm pore diameter AAO membrane infiltrated with photoresist after being etched in an air plasma for 30 min. b) Etch depth plotted against etch time for different pore diameter membranes. Error bars represent the standard deviation of etch depth across samples at a given time point.

After the top surface of the membranes was exposed via the air plasma etch, the membranes were briefly washed (~1 min) in a 5 weight percent solution of phosphoric acid in water, dried in nitrogen, and placed in a vacuum desiccator along with a 200 µL drop of perfluorodecyltrichlorsilane (Fisher Scientific) for three hours. The portions of the pores exposed by the plasma etch bonded with the silane, creating a hydrophobic section. Everywhere the photoresist was still within the pore was protected from silane deposition and remained hydrophilic.

2.5.3 PHOTORESIST REMOVAL AND MEMBRANE BAKE

After silane deposition, the bulk of the photoresist was removed by rinsing the membranes in acetone for 5 min. To ensure any remaining photoresist was removed, the membranes were then rinsed in microstrip 2001 at 60° C for 30 min. Finally, the membranes were baked for approximately 8 hr at 90° C on a hot plate to help align the adsorbed silane molecules as well as evaporate any excess molecules that may have adsorbed to the surface.

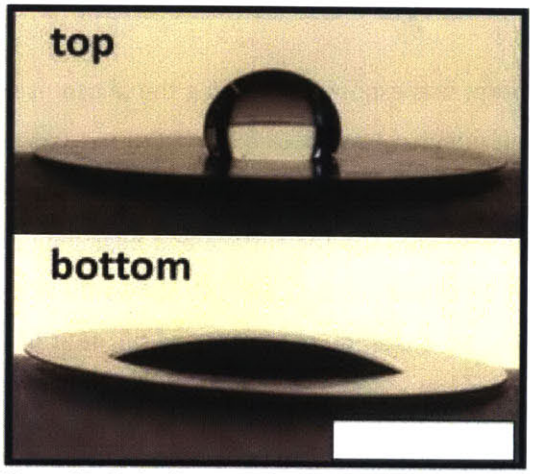

Figure 15: Optical images of a drop of water on the top and bottom surfaces of the biphilic membrane. The bottom is hydrophilic while the top is hydrophobic. (scale bar: 5 mm)

The biphilic nature of the membranes can be seen in Figure 15. The bottom of the membrane remained hydrophilic and was able to wick liquid into the pore and up to the evaporating interface. The top surface, however, was hydrophobic. Therefore, any liquid that wicked into the pore became pinned at the onset of the hydrophobic layer, preventing the pore from flooding and keeping the liquid at a location of known geometry as desired.

2.5.4 BIPHILIC MEMBRANE CHARACTERIZATION

After treatment, the depth into the pore that was made hydrophobic was confirmed via SEM imaging. Before imaging, the pores were filled with a 5 nm gold nanoparticle solution (Sigma Aldrich). The nanoparticle solution was then evaporated from the membrane. While evaporating the solution left behind nanoparticles everywhere it wet the membrane, i.e., the hydrophobic section had no nanoparticles and the hydrophilic section did. It can be seen in Figure 16a and b that the nanoparticles were confined below the hydrophobic layer, and the distance to where the nanoparticles were first found corresponded to the etch depth described previously.

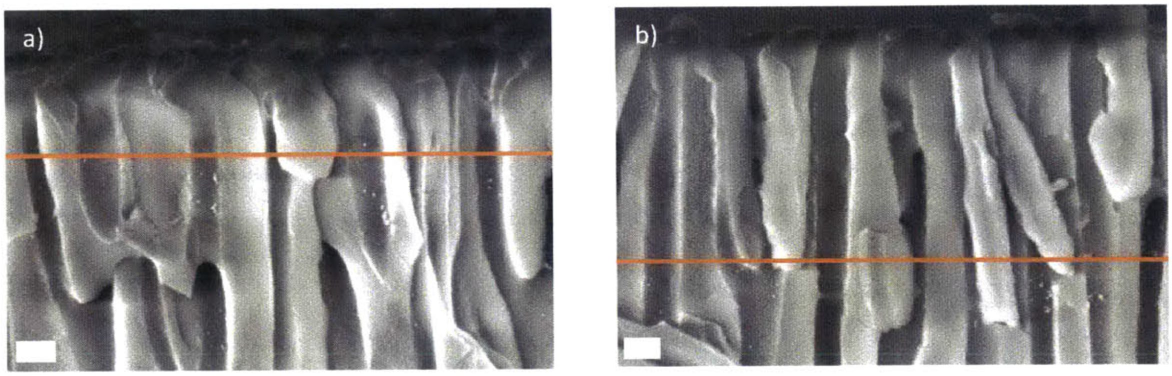

Figure 16: Cross section SEM images of membranes filled with 5 nm gold nanoparticles after biphilic treatment for different photoresist etch times. The onset of the hydrophobic section is shown as an orange line. Gold nanoparticles (appear as bright spots within the pores) are not found within this section but are found below it. a) shorter etch time. b) longer etch time. (scale bars: 100 nm)

2.6 SUMMARY

Starting from AAO membranes, we fabricated nanoporous membranes that can be used to test thin film evaporation from nanopores under a variety of conditions, as well as probe the dependence of heat transfer performance on different geometric parameters of interest based on previous modeling and experimental work. The RTDs and heaters were deposited via E-beam evaporation on the membrane surface to allow measurement of temperature and to supply heat near the evaporating interface. Biphilic membranes were created by infiltrating the membranes with AZ5214. The photoresist was then etched into the pore to expose the top section of the nanopores. This exposed section was made hydrophobic via silanization. The extra photoresist was then removed. The resulting membrane wicked liquid in from the bottom, hydrophilic side; however, the meniscus became pinned at the onset of the hydrophobic layer. This allowed enhanced control over the location of the meniscus within the pore, as well as allowed for improved characterization of the geometry at which the evaporating interface was formed.

3 EXPERIMENTAL SETUP AND PROCEDURE

3.1 GOALS FOR THE EXPERIMENTAL SETUP

The design of the experimental setup was created to allow for testing at conditions relevant to real thermal management devices as well as to ensure accuracy of heat and mass transfer measurements to accurately probe evaporation from nanoporous membranes.

Typical phase change thermal management systems are closed loop systems that reject heat to the ambient environment with a condenser. This sets the condenser temperature at or above the ambient temperature and means evaporation occurs into saturated vapor conditions of a single species. Therefore, all evaporation tests were conducted into saturated vapor at ambient temperature (~22° C).

In order to minimize heating power being dissipated via conduction through the test fixture, an evaporation area of 0.64 cm^2 was used. The larger the evaporation area used the larger the ratio of evaporative heat transfer to conduction heat transfer through the test fixture. Evaporative heat transfer (as defined in Chapter 4) accounted for more than 95% of heat dissipation during experiments.

Previous experimental works have not included the ability to confirm that heat was being dissipated through thin film evaporation within the nanoporous membrane, but instead assumed thin film evaporation based on heat transfer performance. [29-32] Therefore, we included accurate measurements of mass flow rates and visualization of the membrane surface in the experimental setup to confirm the heat transfer regime.

Two figures of merit guide fluid choice for membrane-based evaporative cooling devices. The first figure of merit is the interfacial heat transfer factor in Eq. 1, where h_{fg} is the enthalpy of vaporization, ρ_{sat} is the saturated vapor density, and R is the specific gas constant. All properties are evaluated at 25 °C. A larger interfacial heat transfer factor indicates better interfacial heat transfer. Therefore, fluids with large h_{fg} and ρ_{sat} perform well. [38]

$$\Pi_1 = \frac{h_{fg}\rho_{sat}\sqrt{R}}{h_{fg,water}\rho_{sat,water}\sqrt{R_{water}}} \tag{1}$$

The second figure of merit for fluid choice is the liquid transport factor in Eq. 2, where σ is the surface tension, ρ_l is the liquid density, and μ_l is the liquid viscosity. The larger the liquid transport factor is, the less likely the device is to reach a limited fluid supply regime. [39]

$$\Pi_2 = \frac{\sigma \rho_l h_{fg}}{\mu_l} \Big/ \frac{\sigma_{water} \rho_{water} h_{fg,water}}{\mu_{water}} \qquad (2)$$

Table 1 lists these two figures of merit for water, isopropyl alcohol, and R134a. Water was chosen as a working fluids primarily for ease of use with experimental equipment available for this work, as well as the ability to use it with the biphilic membranes (fluids with low surface tension still wet the section that was supposed to be non-wetting). However, it is noted that other fluids, such as R134a, have significantly larger interfacial heat transfer factors and would exhibit significantly higher heat flux coefficients. These fluids, however, may be more prone to reach the limited fluid supply regime due to the small liquid transport factor. To test the limited fluid supply regime, isopropanol was chosen due to its low liquid transport factor and ease of use with the experimental setup.

Table 1: Interfacial heat transfer factor and liquid transport factor for water, isopropanol, and R134a

Fluids	Water	Isopropanol	R134a
Π_1	1	1.075	42.95
Π_2	1	0.03348	0.05451

3.2 TEST FIXTURE

An exploded view of the test fixture is shown in Figure 17a as well as an optical image with the membrane sealed between the O-rings in Figure 17b. The test fixture was designed to allow for the measurement and quantification of the different mass and heat transfer modes possible (sensible heating of fluid below the membrane, conduction through the test fixture, radiation and convection on the vapor side of the membrane, and evaporation), as well as ensure that evaporation was the dominant mode. Furthermore, the fixture also allowed different membranes to be quickly swapped in and out, enabling simple testing of many different fabricated samples.

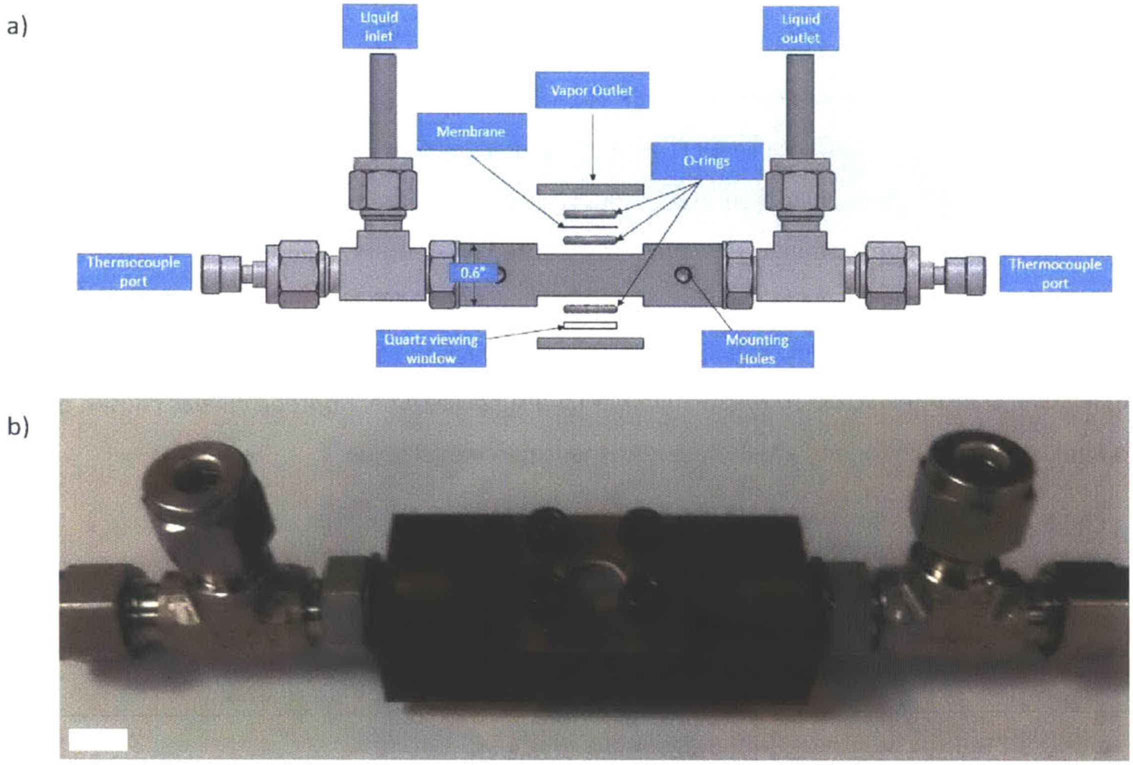
a)
Liquid inlet
Liquid outlet
Vapor Outlet
Membrane
O-rings
Thermocouple port
0.6"
Thermocouple port
Quartz viewing window
Mounting Holes
b)

Figure 17: a) Exploded view of test fixture, depicting fluid inlets and outlets, measurement ports, and membrane location. b) Optical image of test fixture looking down from topside. In the middle the membrane is sealed between two O-rings. (scale bar: 1 cm)

A simplified schematic is shown in Figure 18. The membrane was sandwiched between two O-rings to provide a seal between the liquid side and vapor side. Liquid was flown in at the backside of the membrane, and the temperature of the incoming and outgoing liquid was monitored with thermocouples. (K-type, Omega) Wire leads were clamped against the contact pad by the test fixture, allowing for both measurements of resistance and the input of power for evaporation via Joule heating. A quartz window on the back side of the test fixture allowed for visualization.

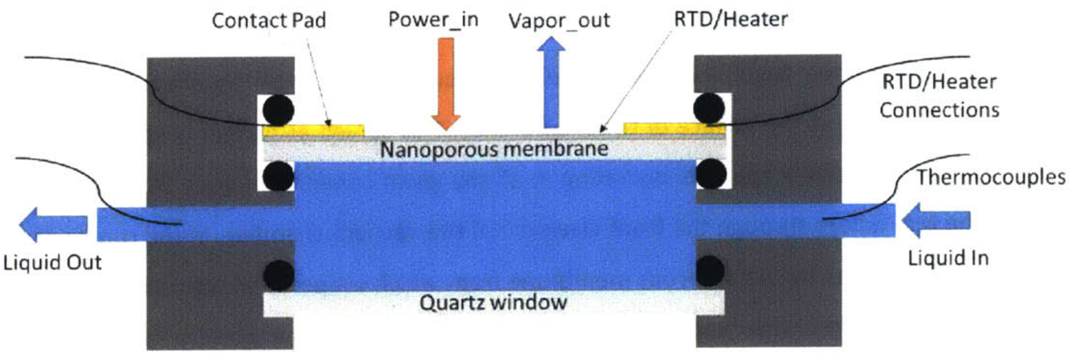
Contact Pad
Power_in
Vapor_out
RTD/Heater
RTD/Heater Connections
Nanoporous membrane
Thermocouples
Liquid Out
Liquid In
Quartz window

Figure 18: Schematic of cross section of test fixture and membrane.

3.3 EXPERIMENTAL SETUP

The test fixture and membrane was then placed inside a vacuum chamber as shown in the schematic and image in Figure 19a and b. The vacuum chamber allowed all air to be evacuated from the chamber, after which the vapor pressure and temperature of the chamber were set for experiments. A reservoir of the working fluid was attached to a pump that fed the liquid through the test fixture. The liquid that exited the test fixture was fed into a balance that accurately recorded the weight. From this weight the liquid flow rate at the exit was known, and the liquid flow rate at the inlet was set by the pump, which was calibrated. Thermocouples (K-type, Omega) at the liquid inlet and outlets, as well as various other thermocouples in the chamber (J-type, Omega) to record the ambient conditions, were connected to a data acquisition device and recorded. The current and voltage supplied by the source-meter were also recorded, from which the input electrical power and RTD resistance was calculated. A light source behind the sample passed light through the quartz window and through the sample, which was collected by a digital camera and macro lens monitoring the surface to provide extra information about the state of the membrane surface.

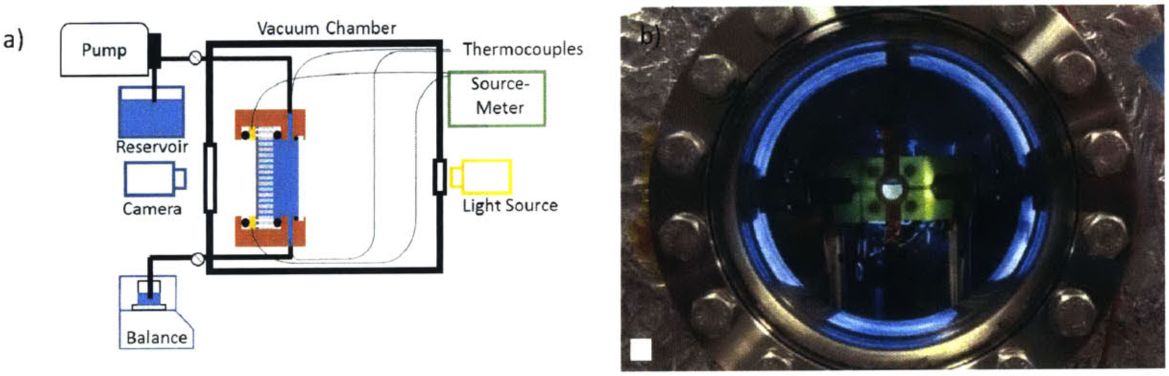
a)
Pump
Vacuum Chamber
Thermocouples
Source-Meter
Reservoir
Camera
Light Source
Balance
b)

Figure 19: a) Schematic of experimental setup. b) Optical image of test setup inside vacuum chamber through camera viewport. (scale bar: 1 cm)

3.4 MEMBRANE VISUALIZATION

Throughout evaporation tests the membrane was visualized in order to shed light on what was happening within and at the surface of the membranes. This served as further confirmation of the heat transfer regime the membrane was operating in at any given condition. Figure 20a showed an optical image of the test fixture through the front viewport of the vacuum chamber. In the center of the image and the test fixture was the nanoporous membrane from which evaporation was occurring. Figure 20b-d show non-biphilic membranes under different heating powers. At low powers the membrane floods completely and a thick film forms on the surface. This regime was called the flooding regime in this thesis (b). Flooding was reduced as power increased and the surface exhibited both flooding portions as well as pore level evaporation regions simultaneously. This regime was called the transition regime in this work (c). Finally, when the heat flux was high enough no flooding remained and all liquid was confined within the nanopore. This regime was called pore level evaporation in this work. (d)

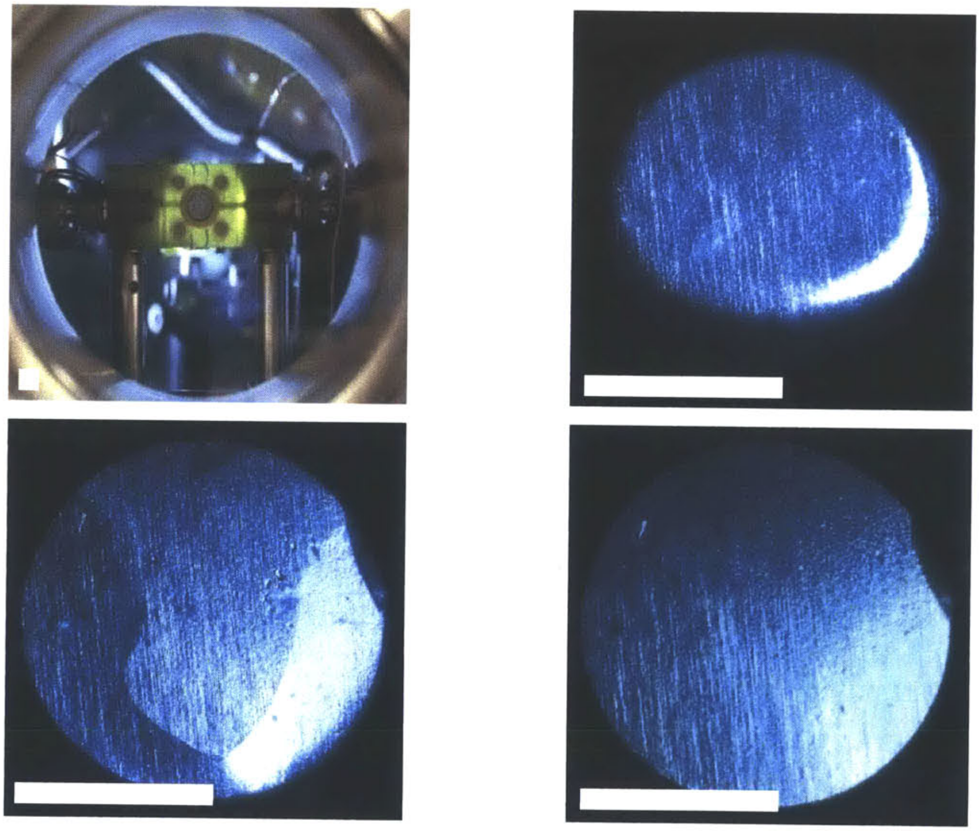

Figure 20: a) Test fixture as seen through camera viewport. b) Membrane flooded with liquid. The dark region at the bottom is a thick layer of liquid building up. c) Membrane where heating of the surface has caused flooding to stop for a portion of the surface but flooding still remains along the bottom and sides of the membrane. d) Heating power is great enough that no flooding remains. (scale bars: 5 mm)

3.5 EXPERIMENTAL PROCEDURE

Before testing, the water or isopropanol was first boiled to remove non-condensable gases and then allowed to cool. The working fluid was then pumped up to the first valve seen in the schematic of the experimental setup, at which point both valves were closed. The entire vacuum chamber was then evacuated down to approximately 1 Pa to remove air from the test fixture and the chamber itself. The working fluid was then added to the chamber directly through a separate valve in order to bring the chamber conditions up to saturation conditions at a set temperature (~22° C). The valve to the pump and liquid reservoir was then opened and the fluid filled the back side of the test fixture. Once full the outlet valve was also opened and liquid was pumped through to the scale. The pressure drop between the scale and the membrane was negligible; therefore, the pressure on the liquid side of the membrane was always very close to 1 atm. The pump was then set at a calibrated flow rate and pumped continuously.

At this point the experiment was ready to begin. Evaporation from the membrane was then tested at different input heating powers as follows. First, the flow rates and temperatures were recorded for two minutes without any heating, at which point the heating was turned on by increasing the supplied current. A constant heating power was maintained until the evaporating surface and inlet and outlet temperature readings reached a constant value. Heating was then turned off and the system was allowed to once again reach its equilibrium state as indicated by all temperatures reading approximately 22 °C. This procedure was then repeated with increased power until the membrane failed. Failure occurred either through boiling on the backside of the membrane (when the boiling point of the fluid at 1 atm was reached, 82.6 °C for isopropanol), dryout of the pores (when capillarity was unable to supply enough liquid to the heated surface and the liquid/vapor interface started to recede into the pore), or the maximum allowable membrane temperature of 65 °C was reached if testing with water.

3.6 SUMMARY

In this chapter, an experimental setup was designed to test evaporation from nanoporous membranes. The setup allowed for the accurate characterization of heat dissipation mechanisms through the measurement of mass flow rates and temperatures of not only the liquid inlets and outlets, but also of fluid that passed through the membrane. Visualization also allowed for confirmation of experimental results.

4 MODELING OF DEVICE PERFORMANCE

A simple thermos-fluidic model was developed to describe the experimental setup as well as the fluid transport through the membranes. This model was used to predict evaporative behavior under a variety of conditions.

4.1 ENERGY BALANCE ON TEST FIXTURE

During experiments temperatures and flow rates of all test fixture inlets and outlets were monitored. A control volume was drawn around the test fixture as seen in Figure 21.

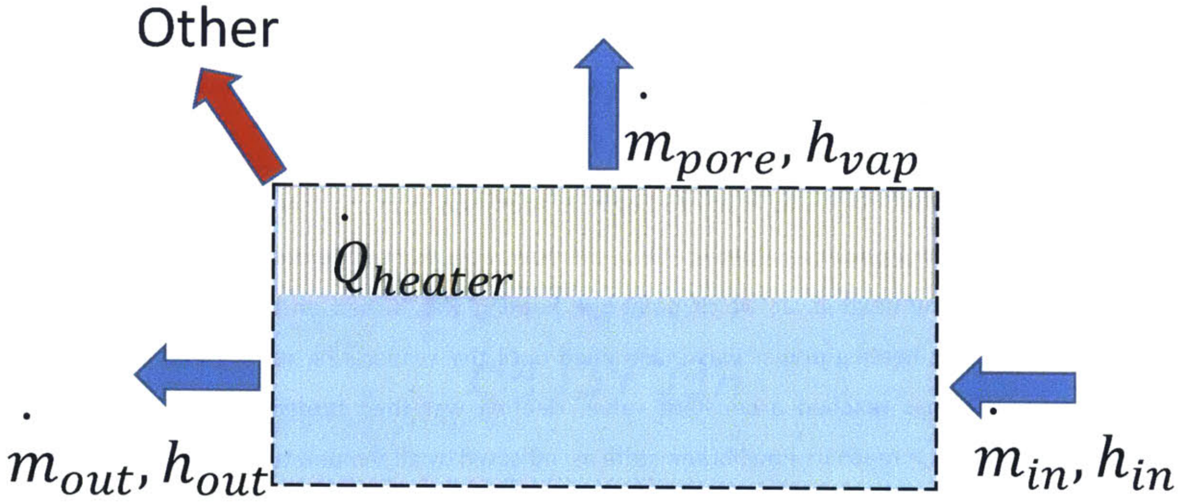

Figure 21: Control volume around test fixture with inlet, outlet, and generation terms.

Using this control volume an energy balance on the test fixture is shown in Eq. 3, where *m* is the mass flow rate, *h* is the enthalpy, and Q_{heater} is the heating provided at the membrane surface via the platinum RTD and heater. *"Other"* in the figure encompasses unmeasured modes of heat transfer such as radiative or convective heat transfer from the membrane surface.

$$\dot{m}_{pore}(h_{vap} - h_{in}) = \dot{Q}_{heater} - (\dot{m}_{out}(h_{out} - h_{in}) + \text{Other}) \qquad (3)$$

Throughout this thesis, $\dot{m}_{pore}(h_{vap} - h_{in})$ was called the evaporative heat flux (Q_{evap}), and Q_{heater} was set during experiments. The term $(\dot{m}_{out}(h_{out} - h_{in}) + Other)$ was characterized experimentally and is called "losses". The losses were characterized by creating a membrane where no liquid or vapor could pass through the pores. Fluid was flown past the back side of the membrane at the same flow rate used in the experiments. The surface was then heated using the platinum heater, and temperature and power were recorded. The results of this characterization are shown in Figure 22. Losses represented less than 5% of the total input heat flux. Data presented in the experimental results section has these losses subtracted from the heater power to determine the evaporative heat flux.

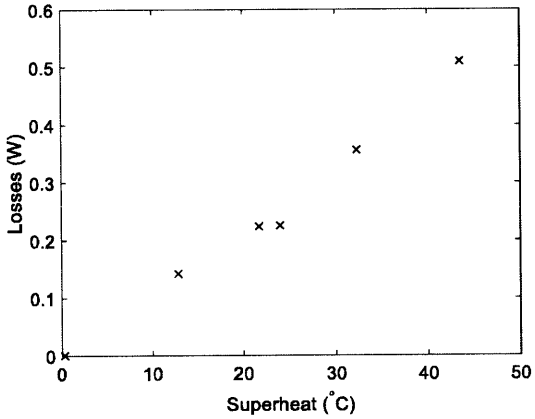

Figure 22: Characterization of losses from test fixture. Loss mechanisms included radiation and convection on the vapor side of the membrane, conduction through the test fixture, as well as sensible heating of the fluid below the membrane.

4.2 FLUID TRANSPORT

In order to reach the evaporating surface the liquid had to first travel through the pores. To model this transport we considered the pores to be cylindrical, and thus began with the Navier-Stokes equation axially along the pore. (Eq. 4)

$$\rho\left(\frac{\partial u_z}{\partial t}+u_r\frac{\partial u_z}{\partial r}+\frac{u_\theta}{}\frac{\partial u_z}{\partial \theta}+\frac{u_z\partial u_z}{\partial z}\right)=-\frac{dP}{dz}+\mu\left(\frac{1}{r}\frac{\partial}{\partial r}\left(r\frac{\partial u_z}{\partial r}\right)+\frac{1}{r^2}\frac{\partial^2 u_z}{\partial \theta^2}+\frac{\partial^2 u_z}{\partial z^2}\right)+g_z \tag{4}$$

Assuming steady state, fully developed flow with axial symmetry, and neglecting gravity this reduced to the following. (Eq. 5)

$$\frac{\partial P}{\partial z}=\mu\left(\frac{1}{r}\frac{\partial}{\partial r}\left(r*\frac{\partial u_z}{\partial r}\right)\right) \tag{5}$$

Solving for the velocity profile in the pore with respect to the radius, and integrating over the radius gave the well-known Hagen-Poiseuille equation relating the pressure drop to the liquid flow rate, where $\Delta P_{viscous}$ is the viscous pressure drop, μ_l is the viscosity, L is the length of the pore, m is the mass flow rate of the liquid through the pore, r_p is the pore radius, and ρ_l is the density. (Eq. 6)

$$\Delta P_{viscous}=\frac{8\mu_l L\dot{m}}{\pi r_p^4\rho_l} \tag{6}$$

Under steady state conditions, this viscous pressure drop needed to be balanced by the pressure budget, which was a combination of the pressure difference across the membrane, as well as any capillary pressure generated at the curved meniscus (Eq. 7). Figure 23 shows a schematic of the different pressures relevant to liquid supply to the evaporating interface, where P_{supply} is the liquid pressure at the backside of the membrane, P_{vapor} is the bulk vapor pressure, P_{vi} is the vapor pressure at the liquid-vapor interface, and P_{li} is the liquid pressure at the liquid-vapor interface.

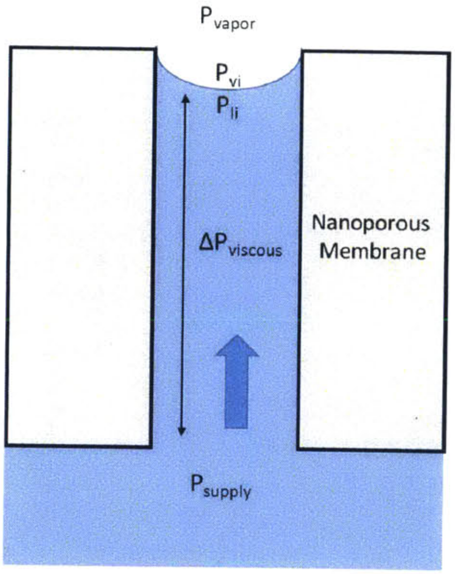

Figure 23: Schematic of different pressures and pressure drops relevant to liquid supply to the evaporating interface

$$\Delta P_{viscous} = \left(P_{supply} - P_{vapor}\right) + \left(P_{vi} - P_{li}\right) \tag{7}$$

The pressure difference generated at the interface is a function of the curvature of the interface as well as disjoining pressure, which arises due to the very small thickness of the film, or rather, the small distance between the liquid-vapor interface and the pore wall. The disjoining pressure becomes more significant as the pore radius becomes smaller. The capillary pressure, however, has been shown to play the dominant role in fluid transport down to pore radii as small as 30 nm. [35] Therefore, the pressure generated at the interface was approximated using the well-known Young's Laplace equation, where γ is the surface tension of the liquid, κ is the surface curvature, $\Pi_{disjoining}$ is the disjoining pressure, and ϑ is the liquid contact angle with the solid. (Eq. 8) The contact angles were taken from the literature. [40]

$$P_{vi} - P_{li} = 2\gamma\kappa + \Pi_{disjoining} \approx \frac{2\gamma\cos(\theta)}{r_p} \tag{8}$$

Finally, we noted that both the viscous pressure drop (Eq. 6) as well as the capillary pressure (Eq. 8) are non-linear functions of the pore radius. The purchased AAO membranes did not have a single pore size, but rather a roughly normal distribution of pore radii. [41] Therefore, a correction was made to the pore radius used in the above equations. If no capillary pressure was generated (for example if the surface is flooded with liquid) then the correction followed Eq. 9, where r is the pore radius, r_{corr} is the corrected radius value used, and σ and μ are the standard deviation and mean value, respectively, of the pore radius distribution, which was found via image processing of SEM images of AAO membranes. For the case where capillary pressure also supplied liquid this correction was slightly more complicated and can be found in the appendix.

$$r_{corr,vi}^{4} = \int_{-\infty}^{\infty} \frac{1}{\sigma\sqrt{2\pi}} \exp\left(-\frac{(r-\mu)^2}{2\sigma^2}\right) r^4 \,\mathrm{dr} \tag{9}$$

In order to confirm the accuracy of this model, the membranes were subjected to a pressure difference of approximately 100 kPa, and the flow rate of water through the pores was monitored. The measured flow rates were compared to the model prediction at a variety of pore radii, and good agreement was found as seen in Figure 24.

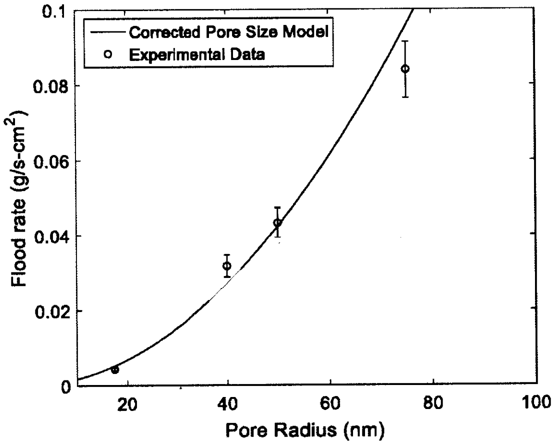

*Figure 24: Membrane flood rate compared to pore radius. Experimental data points are plotted along with the model prediction. Error bars represent the root mean squared error, with the dominant error stemming from uncertainty in the membrane porosity. (*normalized by pore area)*

4.3 MODEL RESULTS

Based on the thermo-fluidic model we predicted three different heat transfer regimes. The first regime occurred when the evaporative heat flux was not enough to evaporate the liquid passing through the porous membrane due to the pressure difference across the membrane. In this situation, the membrane surface flooded as depicted in Figure 25a. In this situation no liquid-vapor interface was within the pore and capillary pressure did not supply liquid. Therefore, liquid was only supplied by the pressure difference between the liquid and vapor sides of the membrane. (Eq. 10) This regime was called the flooding regime.

$$\frac{\dot{Q}_{evap}}{h_{vap} - h_{in}} < \dot{m}_{pore} = f\left(P_{supply} - P_{vapor}, \mu_l, \rho_l, L, r_{corr}\right) \tag{10}$$

When the heating became large enough to evaporate all flooding liquid, the flooding liquid receded into the pore, and additional liquid was brought to the evaporating interface via capillary pressure generated in the nanopores as seen in Figure 25b. As heat flux increased or decreased the interface changed shape in order to bring more or less liquid to the surface to be evaporated. (Eq. 11) This regime was called the pore level evaporation regime.

$$\frac{\dot{Q}_{evap}}{h_{vap} - h_{in}} = \dot{m}_{pore} = f\big((P_{supply} - P_{vapor}), (P_{vi} - P_{li}), \mu_l, \rho_l, L, r_{corr}\big) \tag{11}$$

Finally, when the heat flux became too high for both the pressure difference across the membrane as well as the maximum capillary pressure to supply liquid to the evaporating interface, the meniscus needed to recede as seen in Figure 25c. (Eq. 12) This regime was called the limited fluid supply regime.

$$\frac{\dot{Q}_{evap}}{h_{vap} - h_{in}} > \dot{m}_{pore} = f\big((P_{supply} - P_{vapor}), (P_{vi} - P_{li}), \mu_l, \rho_l, L, r_{corr}\big) \tag{12}$$

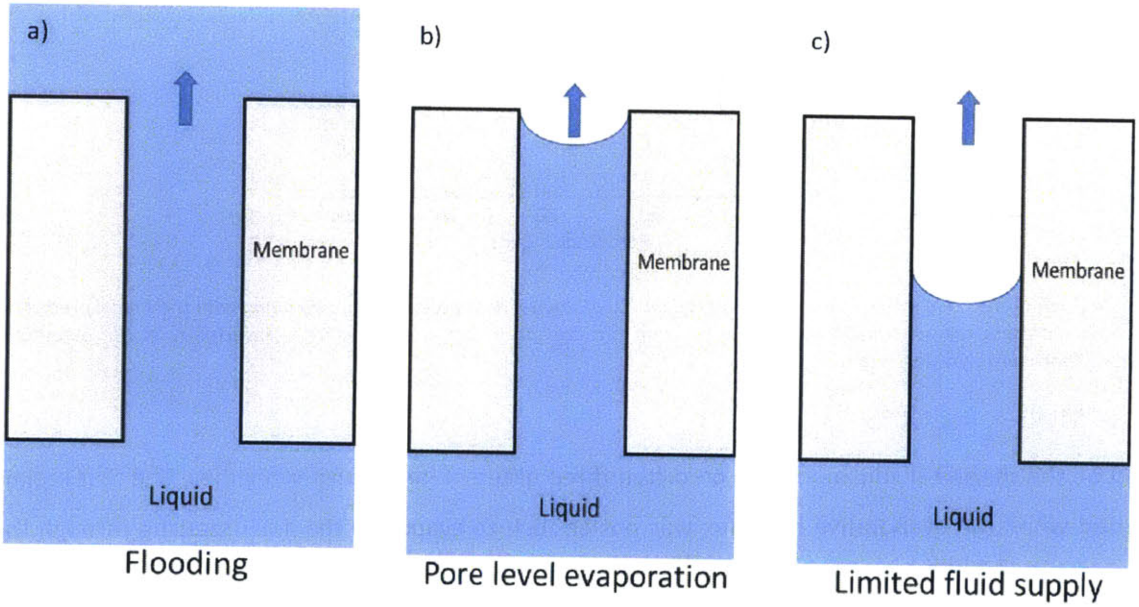

Figure 25: Possible wetting and heat transfer regimes. a) Flooding regime where fluid accumulates on the membrane surface. b) Pore level evaporation regime where fluid supply and evaporation rate balance. c) Limited fluid supply regime where fluid supply is inadequate to supply liquid to the membrane surface.

The transition between each of these regimes was dependent on a number of factors, including membrane geometry (membrane thickness, pore diameter), fluid properties (viscosity, density, enthalpy of vaporization), and system properties (pressure difference between liquid supply and vapor). A regime map of the heat transfer regime as a function of the evaporative heat flux supplied and the pore diameter is shown in Figure 26 for typical experimental conditions used in this thesis (Fluid – Water, T = 22° C, P_{supply} = 1 atm).

The shaded region is the pore level evaporation regime. The boundary between the flooding regime and pore level regime will be called the expected transition in figures in this thesis, and the boundary between the pore level evaporation regime and the limited fluid supply regime will be called the expected limit.

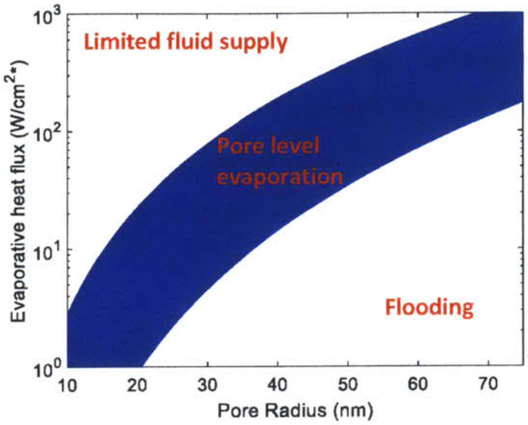

Figure 26: Different heat transfer regimes for evaporation from a nanoporous membrane as a function of the evaporative heat flux and pore radius. (Fluid – Water, T = 22° C, P_{supply} = 1 atm, normalized by pore area)

4.4 SUMMARY

A thermo-fluidic model for evaporation from nanoporous membranes was developed. The model was used to predict heat transfer regimes for evaporation from nanoporous membranes under different conditions. Three possible regimes were predicted, including a flooding regime, pore level evaporation regime, and limited fluid supply regime. The transitions between these regimes were also predicted. In this setup the expected transition to pore level evaporation was set by fluid properties and the pressure difference across the membrane and scaled with r_{corr}^4. At the pore radii considered in this work, the expected limit was dominated by the capillary pressure and scaled roughly with r_{corr}^3.

5 EXPERIMENTAL RESULTS

Based on the predicted heat transfer regimes in Chapter 4, experiments were designed to investigate the heat transfer performance in each regime as well as determine the conditions at which a transition between the regimes occurs. Figure 27 shows experimental data for the evaporation of water from nanoporous membranes with different pore radii and the different heat transfer regimes. A fourth heat transfer regime was identified through experiments and was called the transition regime. Finally, if the evaporative heat flux in Figure 27 were increased enough, the limited fluid supply regime would be reached, but is not shown in this data set. Unless otherwise stated, all experimental conditions in this chapter were evaporation of water into saturated vapor at a temperature of 22° C, a liquid supply pressure of 1 atm, and a membrane thickness of 100 μm.

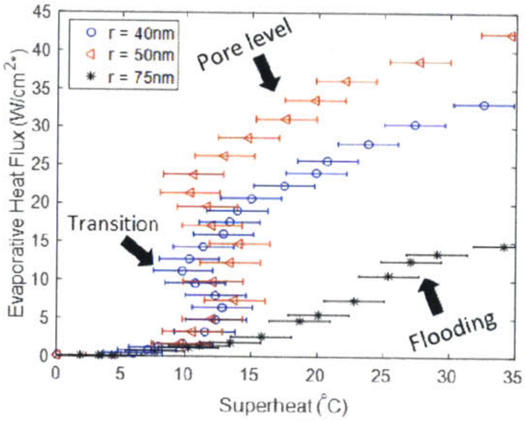

*Figure 27: Evaporative heat flux compared to surface superheat for different pore diameter samples and water as the working fluid. (*normalized by total area)*

In this chapter, we step through each of these regimes and examine the heat transfer performance and mechanism of switching between the regimes. This was done with membranes without biphilic treatment. After this, initial testing with the biphilic membrane was used to examine pore level evaporation in greater detail and to compare the results with a model recently proposed in the literature.

A table of the calculation and sources of error shown in plots in this section is included in the appendix.

5.1 NON-BIPHILIC MEMBRANE EVAPORATION EXPERIMENTS

5.1.1 FLOODING REGIME

The first possible regime was the flooding regime, where the evaporative heat flux was not enough to evaporate all of the liquid being driven through the membrane by the pressure difference between the liquid supply and vapor. In order to test this regime, a large pore radius of 75 nm was used with water as the working fluid, where the predicted transition to a pore level regime was at a much higher evaporative heat flux than what was supplied to the surface. Therefore, more fluid was passing through the pore than could be evaporated, and a thick flooding film formed on the membrane surface as seen in Figure 28a. The darkening of the membrane towards the bottom of the image was caused by the thick liquid layer blocking light from reaching the camera. Figure 28b shows experimental data of the evaporative heat flux compared to membrane surface superheat for the sample with a 75 nm pore radius.

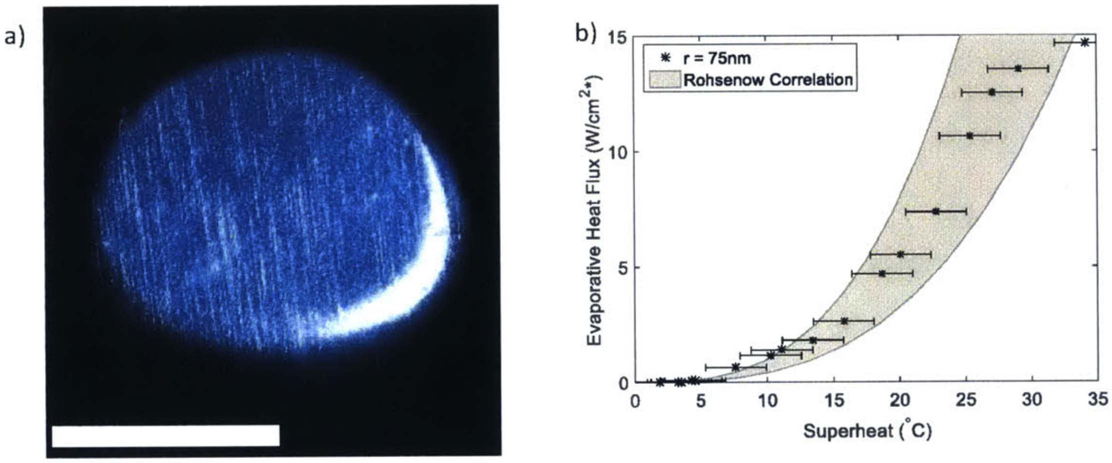

*Figure 28: a) Optical image of membrane in flooding regime. (scale bar: 5 mm) b) Evaporative heat flux compared to membrane surface superheat in flooding regime for 75 nm pore radius sample and water as working fluid. (*normalized by total area)*

Optical visualization as well as the thermo-fluidic model revealed that the membrane was completely flooded and nucleate boiling was occurring on the membrane surface. Therefore, the data in Figure 28b is plotted with the well-known Rohsenow correlation for nucleate boiling, which relates the dissipated heat flux to fluid and surface properties. Values for water and a platinum surface were used. Good agreement was observed.

5.1.2 TRANSITION REGIME

Next, the transition regime was analyzed. This regime was studied by using smaller pore radii, 40 nm and 50 nm, so that the expected transition occurred earlier than for the 75 nm pore radius sample. In

Figure 27, we see that this regime was able to dissipate higher heat fluxes at a given superheat than the boiling regime but was less than that dissipated in the pore level evaporation regime. Surface visualization indicates that this regime occurred when the surface had a combination of the flooding regime and pore level evaporation regime, as shown in Figure 29a. The membrane towards the bottom of the image has a thick flooded film whereas the section at the top of the image has transitioned to pore level evaporation with improved heat transfer. In this experimental setup, this dual behavior occurred due to the thick flooding film periodically falling from the surface due to gravity. As the flooded film fell away, more of the surface transitioned to pore level evaporation, after which the thick film began to form again. Therefore, the membrane surface temperature oscillated between a high and low temperature as the amount of the surface that was flooded oscillated (Figure 29b). As heat flux was increased, the heat flux dissipated approached that of pore level evaporation due to decreases in the portion of the surface that was flooded.

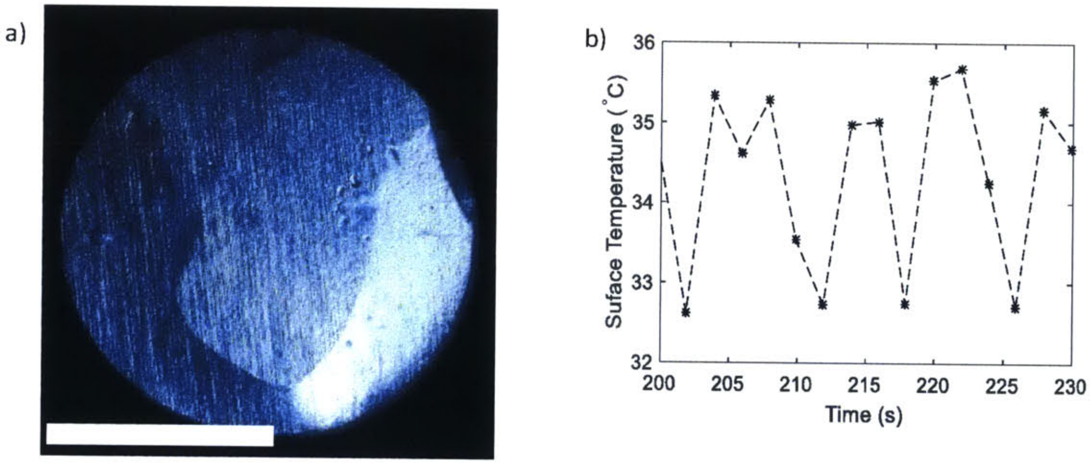

Figure 29: a) Optical image of membrane in transition regime. (scale bar: 5 mm) b) Surface temperature RTD measurements over time for a set heat flux in the transition regime. The surface fluctuates between a high temperature and low temperature as the amount of fluid flooding the surface increases and decreases.

5.1.3 PORE LEVEL EVAPORATION REGIME

The next regime, the pore level evaporation regime, occurred when the heat flux was high enough to prevent all flooding. In order to confirm that this heat transfer regime had been reached, a combination of optical images and analysis using the thermo-fluidic model presented in Chapter 4 was used. The optical image in Figure 30a shows the surface with no visible film flooding the surface, suggesting pore level evaporation had been completely reached. Figure 30b shows an experimentally determined heat flux at the membrane surface using the energy balance in Chapter 4 compared to the actual heat flux delivered via the platinum heater. When in the flooding or transition regime, the energy balance over predicted the heat flux due to fluid passing through the membrane without being evaporated. However, once flooding was completely eliminated and pore level evaporation was reached across the entire surface, the data falls on a 45 degree line, confirming no flooding was present.

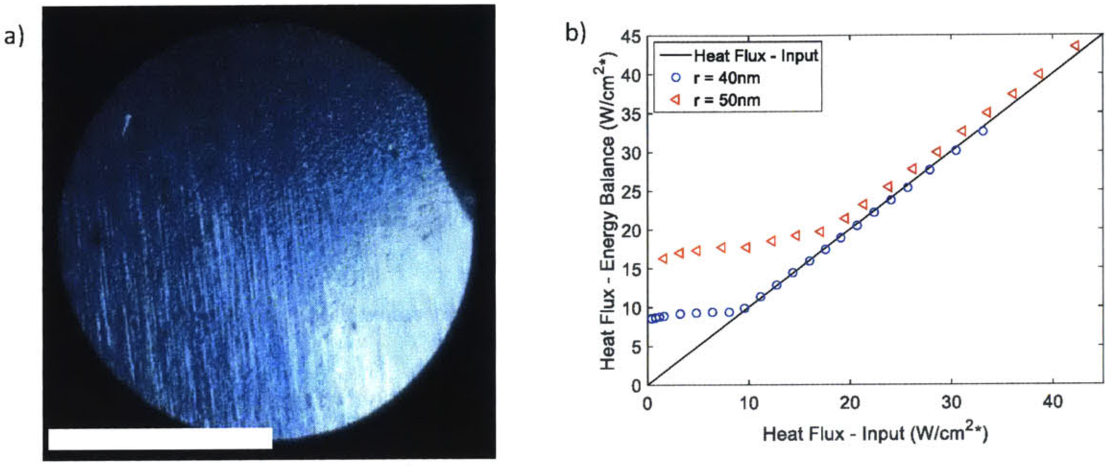

*Figure 30: a) Optical image of membrane surface during pore level evaporation regime. (scale bar: 5 mm) b) Evaporative heat flux determined via an energy balance on the test fixture compared to the heat flux input by the platinum heater. When these data points fall on a 45 degree line thin film evaporation has been reached. (*normalized by total area)*

Figure 31a shows the evaporative heat flux dissipated plotted against surface superheat normalized over the total area as well as the predicted transitions to pore level evaporation from the fluid transport model. Good agreement was observed between the expected transition and when the experimental data suggested a complete transition to pore level evaporation for samples with pore radii of 40 nm and 50 nm. The 75 nm pore radius sample remained in the flooding regime over all input heat fluxes. The 50 nm pore radius sample transitioned to pore level evaporation at approximately 21 W/cm^2, and the 40 nm pore radius sample transitioned near 9.9 W/cm^2. This was consistent with the fluidic model which predicted the transition was dependent on r_{corr}^4 ($\frac{21\frac{W}{cm^2}}{9.9\frac{W}{cm^2}} = 2.121 \approx 2.441 = \left(\frac{50\,nm}{40\,nm}\right)^4$).

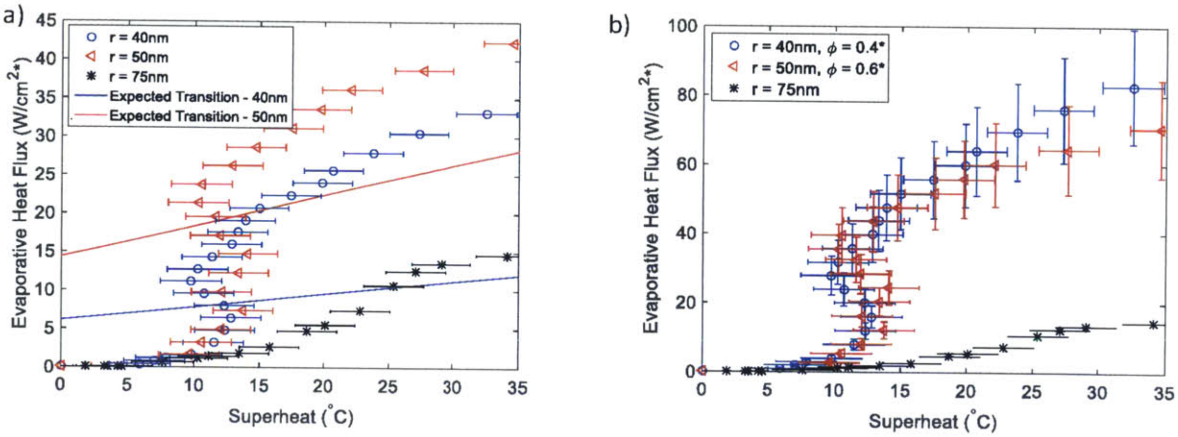

*Figure 31: Evaporative heat flux compared to surface superheat for water evaporated into saturated vapor at 22° C and a supply pressure of 1 atm. a) (*normalized by total area) b) (*normalized by pore area)*

Now that pore level evaporation was reached, we compared heat transfer performance between samples. Therefore, instead of normalizing data by total area, we normalized data by pore area. This was done because evaporation could only occur from the liquid vapor interface, which was confined within the pores. As such, samples of different porosities would be able to dissipate different amounts of heat. The data normalized by pore area, which accounted for the different porosities, is shown in Figure 31b. The membrane porosities were based on the top surface of the membrane and were determined using SEM images. The performance was similar between the 50 nm and 40 nm pore radii samples, but we note large error bars due to the uncertainty in the porosity at the top of the pore stemming from difficulties defining the pore area in SEM images.

Due to the large uncertainty in pore geometry near the membrane surface, as well as flooding, it was difficult to compare samples with different pore radii (for example, the 75 nm pore radius sample remained in the flooding regime). As a result, we developed an approach to create a biphilic membrane as described in Chapter 2.5 to further probe the pore level evaporation regime.

5.1.4 LIMITED FLUID SUPPLY REGIME

In order to probe the limited fluid supply regime, the working fluid was switched from water to isopropanol due to its small liquid transport factor. The reasoning behind this switch is shown in Figure 31a, which shows the heat transfer regimes for both water and isopropanol for various pore radii and evaporative heat fluxes. Isopropanol has a higher viscosity, a lower surface tension, as well as a smaller latent heat of vaporization. These three factors caused isopropanol to switch regimes significantly earlier than water, which allowed experiments to reach the limited fluid supply regime. Once again, the thermo-fluidic model was used to confirm when the samples, one with pore radius of 75 nm and one with a pore radius of 50 nm, transitioned to pore level evaporation. The 50 nm sample transitioned at very low heat fluxes of around 2 W/cm^2, whereas the 75 nm pore radius sample transitioned near 20 W/cm^2, 10 times larger. However, $\left(\frac{75\,nm}{50\,nm}\right)^4$ only equals 5.06. This deviation of the expected transition from r_{corr}^4 was due to the temperature dependence of fluid properties on temperature, where changes in viscosity played the dominant role.

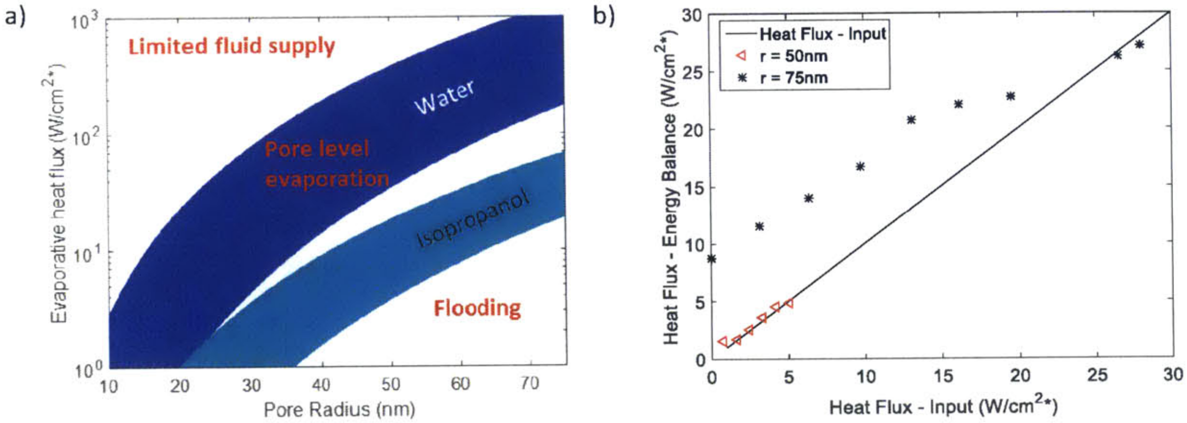

*Figure 32: a) Different heat transfer regimes for evaporation from a nanoporous membrane as a function of the evaporative heat flux and pore radius. (Fluid – Water, Isopropanol, T = 22° C, P_{supply} = 1 atm, normalized by pore area) b) Evaporative heat flux for isopropanol determined via an energy balance on the test fixture plotted against the heat flux input by the platinum heater. When these data points fall on a 45 degree line thin film evaporation has been reached. (*normalized by total area)*

Figure 33 shows the evaporative heat flux normalized over the total area plotted against the surface superheat. The 75 nm pore diameter sample exhibited the multi-regime behavior that was observed for experiments with water. The sample began in a flooded regime with poor heat transfer performance, had a transition region as more and more of the surface reached pore level evaporation, and finally a pore level evaporation regime with the best performance. The transition also occurred near the value predicted by the fluid supply model (solid line), where once again, the upward slope of the expected transition with increasing superheat was due to the dependence of fluid properties on temperature. The expected limit of pore level evaporation is also plotted for the two samples. This line represents where the evaporative heat flux was expected to be too high for the capillary pressure and liquid supply pressure to supply liquid to the surface. The expected limit of the 50 nm pore radius sample was below the heat fluxes being dissipated in the 75 nm pore radius sample. Therefore, even though this sample had transitioned to pore level evaporation around 2 W/cm^2 as seen in Figure 32b, the heat transfer performance did not improve to the level of the 75 nm pore radius sample. We also note that the performance was considerably below the expected limit. This suggests that the fluid supply may not be the only limiting factor, and warrants further investigation if devices based on this concept wish to approach the expected limit. Another limiting factor could be fluid contamination building up near the liquid-vapor interface, reducing evaporation.

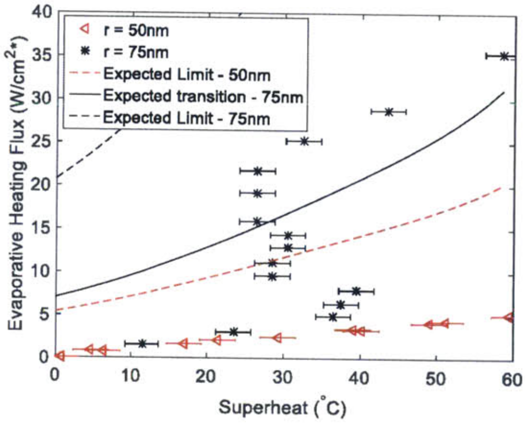

*Figure 33: Evaporative heat flux compared to surface superheat (*normalized by total area) for evaporation of isopropanol into saturated vapor at 22° C with a supply pressure of 1 atm.*

5.2 BIPHILIC MEMBRANE EVAPORATION EXPERIMENTS

Now that the different heat transfer regimes and transitions between them have been investigated, we used the biphilic membrane to examine the pore level regime in more detail. This membrane avoided flooding as well as kept the liquid vapor interface inside the pore where geometry could be more accurately characterized through SEM images. With the biphilic membrane the dependence of pore level evaporation on parameters such as pore diameter, porosity, and meniscus location within the pore can be studied. These tests are ongoing, and initial results of the effect of meniscus location are described here. These results were compared to results predicted by the recent modeling framework developed by Lu *et al*, in which nonequilibrium effects due to deviation from classical kinetic theory were incorporated. [36] The model uses the Hagen-Poiseuille equation for fluid flow through the pore, an interfacial pressure balance to solve for the interface shape, and radiation analogies to describe vapor transport through the pore. The effect of liquid-vapor interface curvature was ignored in these tests as the model was not sensitive to the curvature under these conditions. [34]

5.2.1 EFFECT OF MENISCUS LOCATION WITHIN PORE

By varying the photoresist etch time, the length of pore that was made hydrophobic was varied, which in turn varied the pinning location of the meniscus in the pore. Previous modeling work identified this as an important parameter for heat transfer performance. [36] In this study, biphilic membranes with different hydrophobic section lengths were created. The length of the hydrophobic section was described by the dimensionless number $L^* = \frac{L}{r}$ where L is the length of the hydrophobic section and r is the pore radius. Three different L^* membranes were created, $L^* = 2$, 6.67 and 14.67, and evaporation tests were run with water as the working fluid, vapor saturation conditions at 22° C, and a liquid supply pressure of 1 atm.

Figure 34 shows the evaporative heat flux compared to membrane surface superheat for the three different L^* samples. The evaporative heat flux for a given superheat was higher for the samples with a smaller L^*. This can be explained by the additional vapor transmission resistance due to the hydrophobic section of the pore. As L^* increased, the liquid-vapor interface was further from the membrane surface, and as such, the resistance to vapor transport increased. Any vapor generated needed to first transport through the hydrophobic section of the pore to escape.

The dotted lines were generated using the modeling framework presented in [36]. An accommodation coefficient for the model was chosen by fitting the data from the $L^*=2$ sample, and was found to be approximately 0.18. This value is similar to recent literature on the topic [37]; however, we note that the proper value of the accommodation coefficient has been heavily debated over many decades, with significant variation in reported values. [42-46] Therefore, at this point, this data serves more to confirm trends identified via modeling than determine the exact magnitude of the trends.

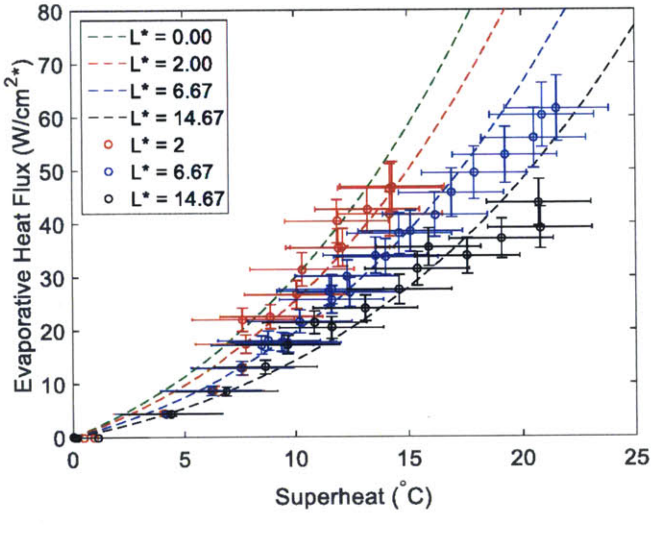

*Figure 34: Evaporative heat flux compared to surface superheat (*normalized by pore area) for evaporation of water into saturated vapor at 22° C with a supply pressure of 1 atm with a biphilic membrane. Tests are run with membranes with three different L*. Dashed lines are from the model framework presented in [36].*

Figure 35 shows the evaporative heat flux normalized by pore area plotted against L^*. The significance of the depth of the pinning location increased as the surface superheat was increased. Furthermore, we note that the evaporative heat flux dropped as the meniscus was moved away from the membrane surface. Little change was seen between samples at 5 °C superheat, but a reduction in evaporative heat flux of 46% was observed between an L^* of 2 and 14.67 at 15 °C superheat. The decrease in heat flux then slowed at higher L^*. The increased importance of the pinning location for high superheats can be explained by considering the resistances to vapor transport as proposed in [37]. The resistance to vapor transport can be approximated by Eq. 13.

$$R_{vapor} = R_{interface} + R_{transmission} \tag{13}$$

At a given L^*, $R_{transmission}$, the resistance to vapor escaping the pore, remained roughly constant for different superheats. $R_{interface}$, the resistance to creating vapor at the interface, decreased with increasing superheat. This is due to a number of reasons, such as the nonlinear dependence of vapor pressure on temperature. Therefore, as superheat was increased, the relative importance of the transmission resistance increased, causing a quicker drop in heat flux for larger superheats.

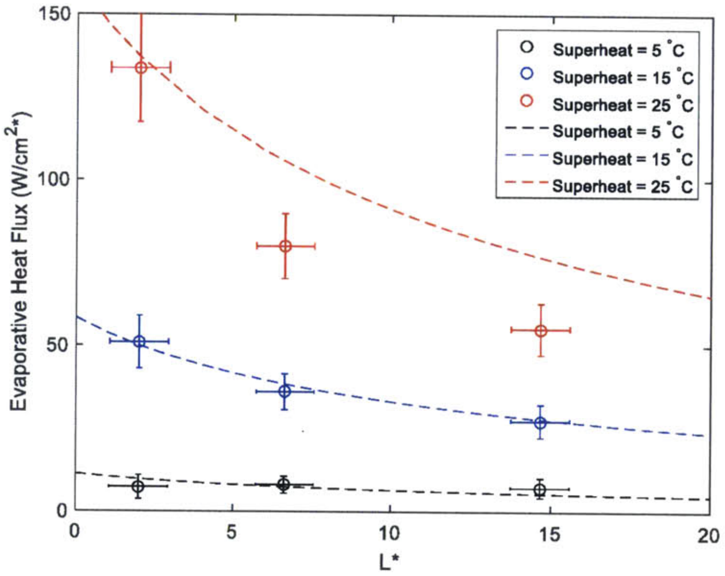

Figure 35: Evaporative heat flux plotted against L for different superheats (*normalized by pore area). Tests are conducted evaporating into saturated vapor at 22° C with a supply pressure of 1 atm with a biphilic membrane. Tests are run on membranes with three different L*. Dashed lines are from the model framework presented in [36].*

5.3 SUMMARY

Four different heat transfer regimes were examined and the transitions between regimes were predicted. The first regime, the flooding regime, had a thick film of liquid on the membrane surface that boiled. The second regime, the transition regime, occurred when the surface was partially in a flooded state and partially in a pore level evaporation state. As heat flux increased, the portion of the surface in the pore level evaporation regime increased, and the heat transfer for a given superheat increased significantly. Next, the pore level evaporation regime occurred when the supply pressure of the liquid was not large enough to provide liquid to the evaporating interface. In this regime, additional fluid supply was brought to the evaporating interface via capillary pressure. This regime had significantly improved heat transfer performance over the other regimes, with a 10 fold increase in heat transfer performance over the flooding regime. The final regime, the limited fluid supply regime, showed that the heat transfer during pore level evaporation was limited below what can be dissipated in the pore level evaporation regime.

Finally, in order to further study pore level evaporation, biphilic membranes were created that prevented flooding and held the liquid at certain locations within the pore. Trends in heat transfer were observed for different L^* values, where the deeper the liquid interface was within the pore, the lower the evaporative heat flux. It was also shown that as superheat increased, the importance of L^* increased.

6 CONCLUSIONS

This thesis has experimentally demonstrated the behavior of evaporation from nanoporous membranes under a variety of conditions. This was done by developing a robust experimental setup capable of measuring/observing heat transfer performance and controlling parameters more rigorously than previous works. It was shown that significant heat transfer performance improvement is achieved by operating in a pore level evaporation regime, and the necessary criteria for reaching pore level evaporation were investigated. This information is valuable for the design of devices based on this concept. Furthermore, the membrane fabrication process and experimental setup developed in this thesis can serve as a basis for future studies in this area looking more closely at the pore level evaporation regime.

6.1 CONTRIBUTIONS

The objective of this thesis was to experimentally investigate evaporation from nanoporous membranes to further enhance both practical and fundamental understanding of the concept. Previous works, both experimental and theoretical, in this area were identified, and a set of experiments were designed to contribute to current understanding.

In Chapter 2 and Chapter 3 a nanoporous membrane with control over a variety of parameters was created. This was done starting with an anodic aluminum oxide nanoporous membrane, depositing a resistance thermometer/heater on the surface, and finally creating a non-wetting section of the pore. This nanoporous membrane was designed side by side with an experimental setup capable of accurately measuring the evaporative heat and mass fluxes. With this setup, parameters that were not previously investigated in detail could be accurately probed.

Simple models describing the experimental setup and liquid transport through the nanoporous membrane were developed in Chapter 4 and used to predict possible heat transfer regimes depending on the different parameters, including working fluid properties such as density, enthalpy of evaporation, and surface tension; membrane properties such as porosity, pore diameter, pore diameter distribution, and membrane thickness; as well as system parameters such as liquid supply pressure and vapor conditions. Predicted regimes were flooding, pore level evaporation, and the limited liquid supply regime.

Experiments were then conducted in Chapter 5, demonstrating heat transfer performance in each of the three regimes, as well as a fourth transition regime that was identified experimentally. In the flooding regime a thick film of liquid formed on the membrane surface and heat transfer occurred through boiling on the surface. This regime occurred when the liquid supply was too great to be evaporated by a given heat flux. The second regime was the transition regime, which was a combination of flooding and pore level evaporation. As such the heat transfer performance was also a combination of the two regimes. This regime occurred due to device specific conditions including membrane orientation and test fixture geometry (in this case gravity removal of flooding liquid). Once a high enough heat flux was reached pore level evaporation was achieved, which demonstrated the best heat transfer performance. The expected transition to this regime matched well with experimental results and can be used in the design of real systems. Finally, a limited fluid supply regime was tested where larger evaporative heat fluxes could not be supported. Poor heat transfer performance was observed compared to samples that were not limited in fluid supply.

Finally, using the biphilic membrane, trends expected in past modelling works were experimentally observed in Chapter 5. It was shown that the location of the meniscus within the pore is an important design parameter, especially at larger superheats.

6.2 RECOMMENDATIONS FOR FUTURE WORK

We plan to use the biphilic membrane to do further testing of pore level evaporation. Modeling works have examined the significance of many parameters, and the membrane fabrication process and experimental setup will not only help test the dependence of pore level evaporation on these parameters, but also serve as a powerful tool in validating the modeling frameworks previously proposed. The two geometric membrane parameters that will be studied in further detail are membrane porosity and pore diameter. It has been suggested that the heat transfer performance of pore level evaporation is insensitive to both of these parameters for evaporation from nanoporous membranes. The proposed studies, as well as the work presented in this thesis, will serve as a valuable starting point for the design of devices based on this concept, as well as for future studies aiming to further increase heat transfer performance and demonstrate ultra-high heat flux dissipation.

7 REFERENCES

1. Pop, E., *Energy dissipation and transport in nanoscale devices.* Nano Research, 2010. **3**(3): p. 147-169.
2. Bagnall, K.R., *Device-level thermal analysis of Gallium nitride-based electronics*, in *Department of Mechanical Engineering*. 2013, Massachusetts Institute of Technology.
3. Wu, Y., et al. *40-W/mm double field-plated GaN HEMTs*. in *Device Research Conference, 2006 64th*. 2006: IEEE.
4. Liu, X., et al., *Thermal management strategies for high power semiconductor pump lasers.* Components and Packaging Technologies, IEEE Transactions on, 2006. **29**(2): p. 268-276.
5. Pautsch, G., *Thermal challenges in the next generation of supercomputers.* CoolCon, May, 2005.
6. Kim, S., et al., *Surface wettability change during pool boiling of nanofluids and its effect on critical heat flux.* International Journal of Heat and Mass Transfer, 2007. **50**(19): p. 4105-4116.
7. You, S., J. Kim, and K. Kim, *Effect of nanoparticles on critical heat flux of water in pool boiling heat transfer.* Applied Physics Letters, 2003. **83**(16): p. 3374-3376.
8. Chen, R., et al., *Nanowires for enhanced boiling heat transfer.* Nano letters, 2009. **9**(2): p. 548-553.
9. Lee, J. and I. Mudawar, *Two-phase flow in high-heat-flux micro-channel heat sink for refrigeration cooling applications: Part II—heat transfer characteristics.* International Journal of Heat and Mass Transfer, 2005. **48**(5): p. 941-955.
10. Kandlikar, S.G., *Fundamental issues related to flow boiling in minichannels and microchannels.* Experimental Thermal and Fluid Science, 2002. **26**(2): p. 389-407.
11. Koşar, A., C.-J. Kuo, and Y. Peles, *Suppression of boiling flow oscillations in parallel microchannels by inlet restrictors.* Journal of heat transfer, 2006. **128**(3): p. 251-260.
12. Lin, L. and R. Ponnappan, *Heat transfer characteristics of spray cooling in a closed loop.* International Journal of Heat and Mass Transfer, 2003. **46**(20): p. 3737-3746.
13. Wang, H., S.V. Garimella, and J.Y. Murthy, *An analytical solution for the total heat transfer in the thin-film region of an evaporating meniscus.* International Journal of Heat and Mass Transfer, 2008. **51**(25): p. 6317-6322.
14. Wayner, P. and C. Coccio, *Heat and mass transfer in the vicinity of the triple interline of a meniscus.* AIChE journal, 1971. **17**(3): p. 569-574.
15. Potash, M. and P. Wayner, *Evaporation from a two-dimensional extended meniscus.* International Journal of Heat and Mass Transfer, 1972. **15**(10): p. 1851-1863.
16. Wayner, P., Y. Kao, and L. LaCroix, *The interline heat-transfer coefficient of an evaporating wetting film.* International Journal of Heat and Mass Transfer, 1976. **19**(5): p. 487-492.
17. Wayner, P., *Effect of thin film heat transfer on meniscus profile and capillary pressure.* AIAA Journal, 1979. **17**(7): p. 772-776.
18. Wayner, P., *Adsorption and capillary condensation at the contact line in change of phase heat transfer.* International Journal of Heat and Mass Transfer, 1982. **25**(5): p. 707-713.
19. DasGupta, S., J. Schonberg, and P. Wayner, *Investigation of an evaporating extended meniscus based on the augmented Young–Laplace equation.* Journal of heat transfer, 1993. **115**(1): p. 201-208.
20. Schonberg, J., S. DasGupta, and P. Wayner, *An augmented Young-Laplace model of an evaporating meniscus in a microchannel with high heat flux.* Experimental Thermal and Fluid Science, 1995. **10**(2): p. 163-170.
21. Wayner, P.C., *Intermolecular forces in phase-change heat transfer: 1998 Kern award review.* AIChE journal, 1999. **45**(10): p. 2055-2068.

22. Wang, H., S.V. Garimella, and J.Y. Murthy, *Characteristics of an evaporating thin film in a microchannel.* International Journal of Heat and Mass Transfer, 2007. **50**(19): p. 3933-3942.
23. Wang, H., J.Y. Murthy, and S.V. Garimella, *Transport from a volatile meniscus inside an open microtube.* International Journal of Heat and Mass Transfer, 2008. **51**(11): p. 3007-3017.
24. Dhavaleswarapu, H.K., et al., *Experimental investigation of steady buoyant-thermocapillary convection near an evaporating meniscus.* Physics of Fluids (1994-present), 2007. **19**(8): p. 082103.
25. Ding, C., et al., *A flat heat pipe architecture based on nanostructured titania.* Microelectromechanical Systems, Journal of, 2010. **19**(4): p. 878-884.
26. Kim, S.S., et al. *Thermal performance of carbon nanotube enhanced vapor chamber wicks.* in *2010 14th International Heat Transfer Conference*. 2010: American Society of Mechanical Engineers.
27. Hsieh, S.-S. and C.-Y. Lin, *Subcooled convective boiling in structured surface microchannels.* Journal of micromechanics and microengineering, 2009. **20**(1): p. 015027.
28. Xiao, R., R. Enright, and E.N. Wang, *Prediction and optimization of liquid propagation in micropillar arrays.* Langmuir, 2010. **26**(19): p. 15070-15075.
29. Narayanan, S., A.G. Fedorov, and Y.K. Joshi, *Gas-assisted thin-film evaporation from confined spaces for dissipation of high heat fluxes.* Nanoscale and Microscale Thermophysical Engineering, 2009. **13**(1): p. 30-53.
30. Narayanan, S., A.G. Fedorov, and Y.K. Joshi, *On-chip thermal management of hotspots using a perspiration nanopatch.* Journal of micromechanics and microengineering, 2010. **20**(7): p. 075010.
31. Narayanan, S., A.G. Fedorov, and Y.K. Joshi, *Heat and mass transfer during evaporation of thin liquid films confined by nanoporous membranes subjected to air jet impingement.* International Journal of Heat and Mass Transfer, 2013. **58**(1): p. 300-311.
32. Xiao, R., S.C. Maroo, and E.N. Wang, *Negative pressures in nanoporous membranes for thin film evaporation.* Applied Physics Letters, 2013. **102**(12): p. 123103.
33. Hanks, D.F., et al. *Nanoporous evaporative device for advanced electronics thermal management.* in *Thermal and Thermomechanical Phenomena in Electronic Systems (ITherm), 2014 IEEE Intersociety Conference on*. 2014: IEEE.
34. Lu, Z., *Design and modeling of a high flux cooling device based on thin film evaporation from thin nanoporous membranes*, in *Department of Mechanical Engineering*. 2014, Massachusetts Institute of Technology.
35. Narayanan, S., A.G. Fedorov, and Y.K. Joshi, *Interfacial transport of evaporating water confined in nanopores.* Langmuir, 2011. **27**(17): p. 10666-10676.
36. Lu, Z., S. Narayanan, and E.N. Wang, *Modeling of Evaporation from Nanopores with Nonequilibrium and Nonlocal Effects.* Langmuir, 2015. **31**(36): p. 9817-9824.
37. Lee, J., T. Laoui, and R. Karnik, *Nanofluidic transport governed by the liquid/vapour interface.* Nat Nanotechnol, 2014. **9**(4): p. 317-23.
38. Lu, Z., et al., *Design and modeling of membrane-based evaporative cooling devices for thermal management of high heat fluxes.* IEEE Transactions on Components, Packaging, and Manufacturing Technology, 2016.
39. Faghri, A., *Heat pipe science and technology*. 1995: Global Digital Press.
40. Redón, R., et al., *Contact angle studies on anodic porous alumina.* Reviews on Advanced Materials Science, 2006. **11**(1): p. 79-87.
41. Manzano, C., J. Martín, and M. Martín-González, *Ultra-narrow 12nm pore diameter self-ordered anodic alumina templates.* Microporous and Mesoporous Materials, 2014. **184**: p. 177-183.

42. Meland, R., et al., *Nonequilibrium molecular-dynamics simulation of net evaporation and net condensation, and evaluation of the gas-kinetic boundary condition at the interphase.* Physics of Fluids (1994-present), 2004. **16**(2): p. 223-243.
43. Marek, R. and J. Straub, *Analysis of the evaporation coefficient and the condensation coefficient of water.* International Journal of Heat and Mass Transfer, 2001. **44**(1): p. 39-53.
44. Li, Y., et al., *Mass and thermal accommodation coefficients of H2O (g) on liquid water as a function of temperature.* The Journal of Physical Chemistry A, 2001. **105**(47): p. 10627-10634.
45. Chodes, N., J. Warner, and A. Gagin, *A determination of the condensation coefficient of water from the growth rate of small cloud droplets.* Journal of the Atmospheric Sciences, 1974. **31**(5): p. 1351-1357.
46. Bonacci, J., et al., *The evaporation and condensation coefficient of water, ice and carbon tetrachloride.* Chemical Engineering Science, 1976. **31**(8): p. 609-617.

8 APPENDIX

ELECTROLYSIS

During evaporation tests, the heating was provided directly at the membrane surface via the platinum RTD and heater. Therefore, the heater came into direct contact with the evaporating liquid. Due to the fact that a voltage is applied across the heater, it is possible that this voltage caused a chemical reaction, such as electrolysis for water. In order to confirm the effects of these reactions could be ignored, tests were run utilizing a nanoporous membrane with a heater that was an open circuit. The open circuit was created by not depositing platinum along the center of the membrane as seen in Figure 36a.

Electrical leads were attached to either side of the membrane and then to a voltage source. Voltage was then increased across the open circuit when the membrane was in air, as well as when the membrane was in the working fluid. The current was measured at each voltage, and is plotted in Figure 36b. It can be seen that current is higher when in the water, and may be associated with electrolysis. However, this amount of current corresponds to only a very small fraction of the power going to electrolysis. As such, it was ignored in interpreting experimental results.

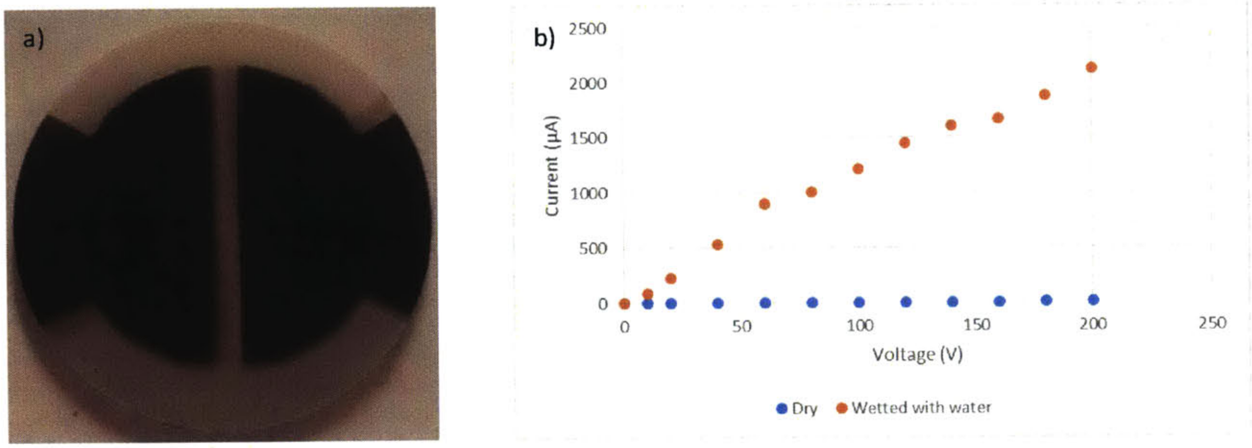

Figure 36: a) open circuit RTD and heater on membrane for electrolysis tests. b) Measured current vs applied voltage during electrolysis tests.

PORE DISTRIBUTION CORRECTION

The correction to the fluid transport model in the flooding regime presented in Chapter 4.2 was only valid for the flooding regime. A different correction must be used in the pore level regime due to the fact that both the pressure difference between the liquid supply and vapor, as well as the capillary pressure are supplying liquid to the surface. These both have different dependences on the pore radius. As such, the correction was somewhat more complicated and is shown in Equation 14.

$$\left(\Delta P + \frac{2\gamma cos\theta}{r_{corr}}\right) r_{corr}^4 = \int_{-\infty}^{\infty} \frac{1}{\sigma\sqrt{2\pi}} \exp\left(-\frac{(r-\mu)^2}{2\sigma^2}\right)\left(\Delta P + \frac{2\gamma cos\theta}{r}\right) r^4 \, \mathrm{dr} \qquad (14)$$

To find the magnitude of this correction, we solved for the mass flow rates through the membrane numerically utilizing the real pore distribution of the membranes and compared it to the flow rate for a membrane of equal porosity with only one pore size. This is shown in Figure 37, where the yellow curve represents the correction to the mass flow rate as a function of pore radius for a 100 kPa pressure difference across the membrane. We see that the correction is a combination of the flooding correction in blue and the capillary correction in orange. At very small pore sizes, the capillary pressure is dominant and so the correction is close to the capillary correction. At larger pore sizes the supply pressure driven flow becomes more and more important as the capillary pressure becomes smaller.

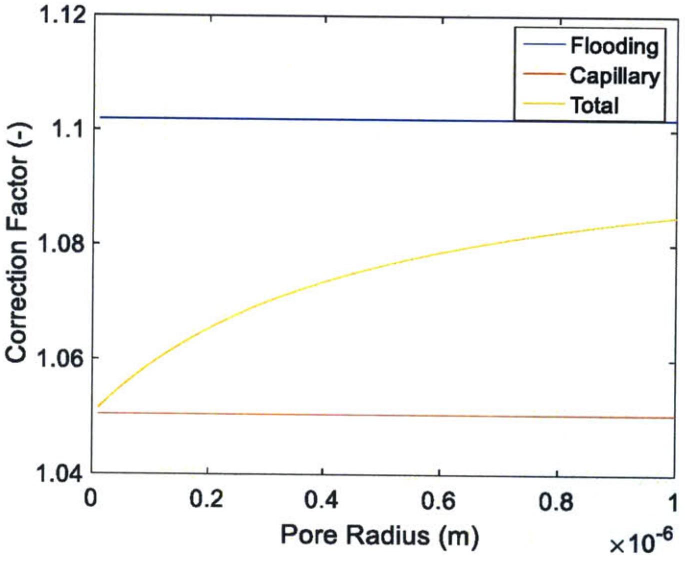

Figure 37: Mass flow rate corrections for a normal pore distribution with a standard deviation of 13% of mean pore radius. Blue is for purely flooding case. Orange is for purely capillary driven flow. Yellow is for a combination of capillary and supply pressure driven flow (Eq. 12).

NON-CIRCULAR CROSS SECTION

As can be seen in the various SEM images of the nanoporous membranes, the pores are not perfectly cylindrical. This can affect both the viscous pressure drop, as well as the capillary pressure generated by the interface, both of which can affect the fluid supply to the evaporating interface. Therefore, Figure 38 shows the ratio of the pressure drop, capillary pressure, and resulting flow rate of an ellipse shaped pore to that of a circular pore of equal cross sectional area for a variety of a/r (where r is the circle radius and a is one axis (minor or major) of the ellipse). We see that the capillary pressure generated by an ellipse is greater than a circle; however, the change in viscous pressure drop is even larger. Therefore, the resulting flow rate in an ellipse is less than that for a pore of circular cross section. This may be a reason for the discrepancy in data and modeling in Figure 24.

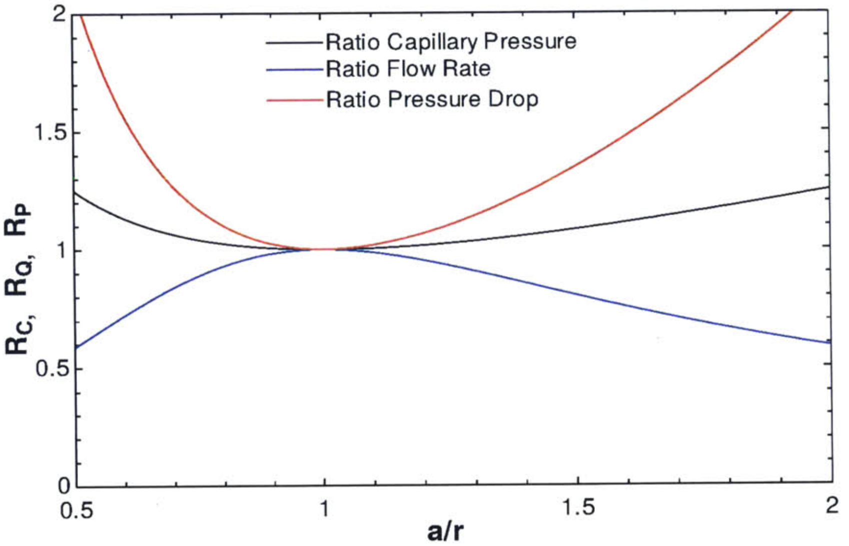

Figure 38: The ratio of the capillary pressure, viscous pressure drop, and fluid flow rate in an elliptical pore to that of a circular pore of the same cross section as a function of the ratio of one axis of the ellipse to the radius of the circle.

BOILING SUPRESSION WITHIN PORE

The surface temperature of the membrane often rose above the boiling point of the liquid within the pore, but boiling did not occur within the pore. This can be explained through an estimation of the superheat necessary to generate a liquid vapor interface via boiling within the pore, using the Young-Laplace equation and the Clausius-Clapeyron equation.

$$P_v - P_l \approx 2\frac{\gamma}{R} \quad \text{Young-Laplace equation}$$

$$\frac{\Delta P}{\Delta T} \approx \frac{h_{fg}\rho_v}{T_{sat}} \quad \text{Clausius-Clapeyron equation}$$

Combining these two equations together yields the following equation:

$$\Delta T \approx \frac{2\gamma T_{sat}}{R h_{fg}\rho_v} \approx O(10{,}000\ K)$$

When plugging in typical values for water in this experimental setup this suggests the boiling superheat necessary to generate bubbles within the pore is very large.

VAPOR FLOW REGIME

The modeling framework presented by Lu *et al.* assumes ballistic transport of vapor molecules within the pore. [36] Therefore, the mean free path of molecules within the pore was confirmed using the equation below, where λ is the mean free path, R is the ideal gas constant, T is the temperature, d is the molecule diameter, N_a is Avogadro's Number, and P is the pressure. Figure 39 shows the Knudsen number (λ/pore diameter) for 150 nm, 100 nm, and 80 nm pore diameter samples. For all experimental tests compared to modeling work developed by Lu *et al.* had Knudsen numbers near of larger than 10, ensuring the accuracy of the ballistic transport assumption.

$$\lambda = \frac{RT}{\sqrt{2}\pi d^2 N_A P} \quad \text{Mean Free Path for Ideal Gas}$$

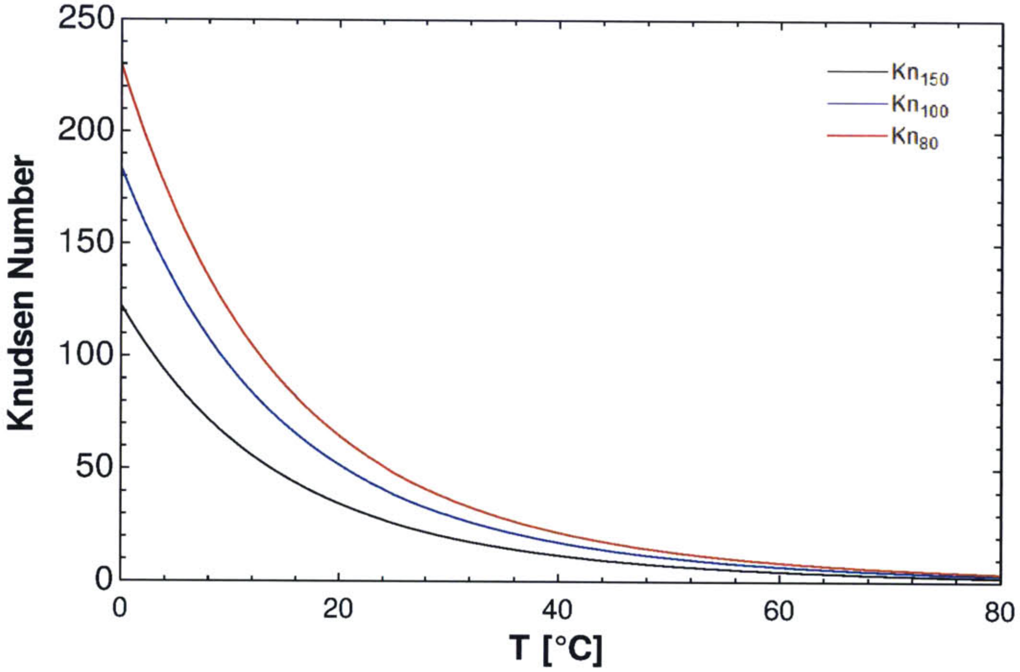

Figure 39: Knudsen number for 150nm, 100nm, and 80 nm pore diameter samples for different temperatures. The Knudsen number was 10 or higher for most tests, ensuring the accuracy of the ballistic transport assumption.

MEMBRANE PARAMETERS

Table 2: Membrane parameters of AAO membranes that can be purchased from Synkera Technologies, Inc.

Parameter	**Standard**						**Custom**
Pore Diameter, nm (SD 7-10%)	18	35	55	80	100	150	10-200
Pore Density,§ cm^{-2}	$6 \cdot 10^{10}$	$1 \cdot 10^{10}$	$6 \cdot 10^{9}$	**$2 \cdot 10^{9}$ §**	**$2 \cdot 10^{9}$,§** $9 \cdot 10^{8}$	**$2 \cdot 10^{9}$,§** $9 \cdot 10^{8}$	$2 \cdot 10^{11}$ - $9 \cdot 10^{8}$
Pore Period,§ nm	44	94	143	**243 §**	**243,§** 367	**243,§** 367	20 - 367
Estimated Porosity,§ %	15	13	13	**10 §**	**15,§** 7	**35,§** 15	10% to 50%
Thickness, µm (± 2%)	50 and 100*						15-150 ± 2%
Format / Size	round shape: 13, 25, 47 mm square shape: 10x10 mm						custom shapes, up to 120 mm in size
Operating Temperature	**No heat treatment:** · up to 500°C (depending on the environment) **Heat treatment options:** · OPTION 1: ≤ 700°C (amorphous) · OPTION 2: ≤ 900°C (γ-alumina) · OPTION 3: ≤ 1000°C (γ/ α - alumina) *						up to 1000°C (γ/ α - alumina) *
Availability	4-6 weeks if not in-stock						Varies

CALCULATION OF ERROR

Throughout this thesis plots showing experimental results have used error bars. This section serves to explain the calculation of these different error bars for the different axes used.

Table 3: Sources and calculation of error for figures presented in thesis.

Axis	**Calculation of error**
Superheat	Error shown is the root mean square error, where the dominant source of error was from the thermocouples used to calibrate the sample RTD. Other sources were error in measuring sample resistance.
Evaporative Heat Flux – Normalized by Total Area	No error is plotted as it is very small. The input power and total projected area of the evaporating surface were well known.
Evaporative Heat Flux – Normalized by Pore Area	Error shown is the root mean square error, where the dominant source of error was due to the uncertainty in sample porosity (~10%). Other sources of error were variation between tests and uncertainty in heating power.
L^*	Error shown is the standard deviation of L^* based on the etch depths of the photoresist during the air plasma etch.
Flood Rate – Normalized by Pore Area	Error shown is the root mean square error, where the dominant source of error was due to uncertainty in the sample porosity (~10%). Other sources of error were measurement error of the scale and uncertainty in fluid density.
Etch Depth	Error shown is the standard deviation of etch depth found across samples at that etch time.